HHS Public Access

Author manuscript

Acta Biomater. Author manuscript; available in PMC 2020 August 01.

Published in final edited form as:

Acta Biomater. 2019 August ; 94: 204–218. doi:10.1016/j.actbio.2019.04.057.

Two-photon Polymerized Poly(caprolactone) Retinal Cell Delivery Scaffolds and their Systemic and Retinal Biocompatibility

Jessica R. Thompson[#,1,2], **Kristan S. Worthington**[#,1,2], **Brian J. Green**[3], **Nathaniel K. Mullin**[1], **Chunhua Jiao**[1], **Emily E. Kaalberg**[1], **Luke A. Wiley**[1], **Ian C. Han**[1], **Stephen R. Russell**[1], **Elliott H. Sohn**[1], **C. Allan Guymon**[3], **Robert F. Mullins**[1], **Edwin M. Stone**[1], **Budd A. Tucker**[1]

[1]Institute for Vision Research, Department of Ophthalmology and Visual Science, Carver College of Medicine, The University of Iowa, 4111 Medical Education and Research Facility, Iowa City, IA 52242, USA

[2]Department of Biomedical Engineering, The University of Iowa, 5601 Seamans Center, Iowa City, IA 52242, USA

[3]Department of Chemical and Biochemical Engineering, The University of Iowa, 4133 Seamans Center, Iowa City, IA 52242, USA

Abstract

Cell replacement therapies are often enhanced by utilizing polymer scaffolds to improve retention or direct cell orientation and migration. Obstacles to refinement of such polymer scaffolds often include challenges in controlling the microstructure of biocompatible molecules in three dimensions at cellular scales. Two-photon polymerization of acrylated poly(caprolactone) (PCL) could offer a means of achieving precise microstructural control of a material in a biocompatible platform. In this work, we studied the effect of various formulation and two-photon polymerization parameters on minimum laser power needed to achieve polymerization, resolution, and fidelity to a target 3D model designed to be used for retinal cell replacement. Overall, we found that increasing the concentration of crosslink-able groups decreased polymerization threshold and the size of resolvable features while increasing fidelity of the scaffold to the 3D model. In general, this improvement was achieved by increasing the number of acrylate groups per prepolymer molecule, increasing the acrylated PCL concentration, or decreasing its molecular weight. Resulting two-photon polymerized PCL scaffolds successfully supported human iPSC derived retinal progenitor cells in vitro. Sub-retinal implantation of cell free scaffolds in a porcine model of retinitis pigmentosa did not cause inflammation, infection or local or systemic toxicity after one month. In addition, comprehensive ISO 10993 testing of photopolymerized scaffolds revealed a favorable biocompatibility profile. These results represent an important step towards

Corresponding Author: Budd A. Tucker, 375 Newton Rd., Iowa City, IA, 52242, 319-335-4488, Budd-tucker@uiowa.edu.
[#]These authors contributed equally to this manuscript

understanding how two-photon polymerization can be applied to a wide range of biologically compatible chemistries for various biomedical applications.

Inherited retinal degenerative blindness results from the death of light sensing photoreceptor cells. To restore high-acuity vision a photoreceptor cell replacement strategy will likely be necessary. Unfortunately, single cell injection typically results in poor cell survival and integration post-transplantation. Polymeric biomaterial cell delivery scaffolds can be used to promote donor cell viability, control cellular polarity and increase packing density. A challenge faced in this endeavor has been developing methods suitable for generating scaffolds that can be used to deliver stem cell derived photoreceptors in an ordered columnar orientation (i.e., similar to that of the native retina). In this study we combined the biomaterial poly(caprolactone) with two-photon lithography to generate a biocompatible, clinically relevant scaffold suitable for retina cell delivery.

Graphical Abstract

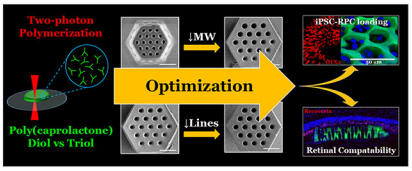

Keywords

Two-Photon Lithography; Biocompatible; Retinal Cell Delivery Scaffold; Patient iPSC Derived Retinal Progenitor Cells; Retinal Transplantation

---

Tissue engineering is based on the principle that environmental cues, both physical and chemical, can direct cell behavior.[1] Material properties such as chemistry, degradability, and stiffness affect the success of a tissue scaffold; thus polymeric materials, which can be readily modified are often suitable for tissue engineering.[2, 3] Polymers, both degradable and non-degradable, have been widely used in regenerative medicine for applications ranging from vascular stents to resorbable sutures and drug delivery devices.[4] As patient-derived induced pluripotent stem cells (iPSCs) and genome editing technologies, such as CRISPR, have advanced to the point where the field of personalized regenerative medicine is now posible, the need to exert precise control over polymer architecture in tissue engineering applications is essential.[5]

Retinal regeneration is one area that could be substantially impacted by the ability to create cellular scaffolds with specific geometries. Blindness caused by retinal degenerative diseases, such as age-related macular degeneration and retinitis pigmentosa, results from death of the light sensing photoreceptor cells of the outer neural retina (Figure 1A–B).[5, 6] Although these diseases affect millions of people worldwide, to date no treatments exist for restoring vision due to cellular loss and tissue atrophy.[6, 7] To restore useful vision, a stem cell-derived photoreceptor cell replacement strategy is an attractive option. However, functional tissue scaffolds are likely to be required in order to increase the number of viable cells delivered to the retina and to promote post-transplantation cell survival, proper photoreceptor cell alignment and functional integration (Figure 1C).[8–10] To date, several

polymers have been investigated pre-clinically as retinal cell delivery scaffolds, one of the most promising of which is poly(caprolactone) (PCL).[8, 11–13]

PCL is a degradable polyester that has been used extensively in several biomedical applications including drug delivery,[14] bone and other tissue engineering,[15–18] and to prevent post-surgical adhesion in the peritoneal cavity.[19] PCL is often selected because of its biologically favorable rheological and viscoelastic properties,[20] which make it relatively easy to manipulate into scaffolds and structures with a wide range of properties.[21, 22] Additionally, PCL is well-tolerated in part because of its known slower degradation time than other common degradable polyesters such as poly(lactic acid) and poly(glycolic acid).[13, 20, 23–26] This slower degradation has been shown to decrease cellular toxicity *in vitro* and produce better outcomes *in vivo*, like increased vascularization and reduced inflammation. These advantages are attributed directly to distinct differences in local acidity. For instance, in a side-by-side comparison, the biomaterial environment is substantially more neutral (i.e., less acidic) for PCL than for PLGA [49]. Thus, PCL has been thoroughly investigated in the context of retinal tissue engineering. *In vitro*, linear PCL has been demonstrated to be compatible with neural retinal cells when used on its own[27, 28] or when blended with chitosan[29] or silk fibroin and PLA[30]. Moreover, several groups have demonstrated that linear PCL, particular when electrospun, is a favorable Bruch's membrane mimic, serving as a helpful substrate for RPE cells[31, 32]. Linear PCL is also well-tolerated by retinal tissue *ex vivo* in wild-type mouse[28] and pig,[33] as well as *in vivo* in wild-type pig,[25] rabbit, [34] and rat,[35] as well as a rat model of retinal degeneration.[36] Moreover, photopolymerized PCL, which is crosslinked, does not elicit adverse effects in a wild-type pig retina, and also supports the attachment and proliferation of human iPSCs, which could later be differentiated to retinal precursors.[26]

While surface patterned PCL has also been used to organize and differentiate murine retinal progenitor cells *in vitro*,[12] additional three-dimensional (3D) control of the scaffold structure is necessary to customize this material for human photoreceptor cell replacement therapies. In the human retina, photoreceptor cells are tightly packed at a density of 80,000 - 320,000 cells per mm^2, depending on eccentricity, and perfectly aligned with the path of light entering the eye.[37] These cell density and alignment characteristics are critical for high acuity visual function.[38–40] Thus, a scaffold that facilitates these properties by providing size-relevant 3D physical cues is essential for successful photoreceptor cell replacement therapy.

Photopolymerization-based 3D printing provides a high resolution method of fabrication for finely structured biomaterials. Yet, even with focused lasers, traditional photopolymerization occurs along the entire path of light, limiting the resolution to approximately 50 μm.[26] This translates to even the most precise structures being roughly five times larger than a single photoreceptor cell. Two-photon polymerization is an alternative technique that offers resolution up to three orders of magnitude higher than traditional photopolymerization.[41–43] As its name suggests, this method requires that two photons, each carrying half the activation energy necessary for excitation, combine with a photoinitiator to induce cleavage.[41–43] The photons must reach the initiator within 1 femtosecond of each other, an event

that is exceptionally rare anywhere other than the focal point of the laser. Thus, this process enables precise polymerization of features as small as 50 nm. [41–44]

In this work, we describe the potential of two-photon lithography for high resolution photopolymerized PCL microstructures and evaluate factors that optimize these materials for photoreceptor cell replacement therapies. In our previous studies, we identified an optimal design for photoreceptor cell scaffolds and showed that non-degradable materials fabricated according to the design facilitate photoreceptor packing and vertical alignment. Here, we used a similar approach to create degradable photoreceptor cell delivery scaffolds using two-photon polymerization. We modified PCL with acrylate groups at varying degrees of functionality and molecular weight, while also evaluating the effect of PCL and photoinitiator concentration. Importantly, the addition of acrylate groups allowed PCL to undergo photopolymerization, enabling spatial and temporal control of the resulting structure. For each formulation, we varied laser scanning speed and power to determine the two-photon polymerization threshold. At fixed and optimized two-photon scanning speed and laser power for each formulation, we also varied the hatching and slicing distances of the modeled scaffolds to study design-to-structure fidelity and the ability to scale-up to translationally relevant structures. Lastly, we evaluated scaffold biocompatibility via both contract research organization (CRO) based ISO 10993 testing under good laboratory practices (GLPs), *in vitro* human iPSC-RPC loading and sub-retinal implantation in a pig model of inherited retinal degeneration. Collectively, these results lay the groundwork for applying two-photon polymerization to degradable polymer systems for applications such as retinal regeneration where precise control of material micro-architecture is required.

Materials and Methods

Formulation

To prepare samples for photopolymerization, functionalized PCL prepolymers, which were synthesized by reacting PCL diol and triol with acryloyl chloride (Sigma-Aldrich, St. Louis, MO; see Supplemental Materials and Methods), were dissolved in dioxane (Sigma-Aldrich) to form PCL:dioxane solutions (Ratios of 3:1, 1:1, 1:3). A photoinitiator, 2-Benzyl-2-dimethylamino-1-(4-morpholinophenyl)-butanone-1 (commonly known as Irgacure 369 or I-369, Ciba Specialty Chemicals, BASF, Ludwigshafen, Germany) was added to the solution (at 1, 3, and 5 wt%).

Two Photon Polymerization

3D models were created in AutoCAD 2015 (Autodesk Inc., San Rafael, CA). Describe version 2.2.1 (Nanoscribe GmbH; Eggenstein-Leopoldshafen, Germany) was used to slice and hatch the models. “Slicing” refers to the process of dividing a 3D solid model into a series of horizontal layers, where the distance between each of these layers is defined as the slicing distance. On the other hand, “hatching” refers to dividing each horizontal layer into a series of 2D line commands that are separated by a defined distance known as the hatching distance. After slicing and hatching, the resulting code file was used to vary laser power and scanning speed. Sample preparation is described in greater detail in the Supplemental Information. Each specimen was printed using a Nanoscribe Photonic Professional GT two-

photon lithography system (Nanoscribe GmbH) via regular 3D direct-laser-writing with a 25X objective (NA = 0.8).

Scanning Electron Microscopy

Two-photon polymerized samples were coated with a gold-palladium mixture using an argon beam K550 sputter coater (Emitech Ltd.; Kent, England). Images were collected with a 1.0kV accelerating voltage at suitable magnifications for the model size using a Hitachi S-4800 scanning electron microscope (Hitachi High-Technologies; Ontario, Canada). For scaffolds, images were also collected with a 30° tilt applied to the stage.

Threshold and Resolution

A 10 μm wide (point-to-point) by 1 μm tall star was designed with a 0.1 μm slicing distance and 0.1 μm hatching distance. Based on previously published optimizations, hatching type was fixed as parallel lines with the direction alternating by 90° between each layer.[44] For each formulation, attempts to form this star were performed using laser power ranging from 2% to 100% in increments of 2% and scanning speeds ranging from 6 mm/s to 40 mm/s in increments of 2 and 60 mm/s to 160 mm/s in increments of 20 mm/s. The presence of the stars was determined qualitatively. The minimum laser power at which a star was present was deemed the polymerization threshold. At the fastest scanning speed that did not result in undesirable artifacts, the width (point-to-point) of each star near the polymerization threshold was measured in triplicate using image analysis (ImageJ 1.48v) of scanning electron micrographs.

Scaffold Fidelity to Model

Generic scaffolds were designed as previously described.[44] Briefly, each scaffold had 20 μm diameter vertical pores intended to house cells and 7 μm diameter horizontal pores intended to allow fluid and nutrient transport. For each formulation, the optimum scanning speed and laser power were selected based on the conditions that resulted in stars with widths closest to the model (see experimental design above). The slicing distance was held constant at 0.5 μm while the hatching distance was manipulated: 0.1, 0.5, 1.0, and 1.5 μm. Likewise, the hatching distance was held constant at 0.5 μm while the slicing distance was manipulated: 0.1, 0.5, 1.0, and 1.5 μm. The diameter and roundness of the vertical pores, as well as the scaffold width and height, were evaluated using SEM and ImageJ, as described in detail in the Supplemental Information.

The quality of the horizontal pores was determined using a 4-point scale (0 – 3) with zero representing a complete absence of pores and three representing pores that appeared to traverse the full width of the scaffold, see Figure S3 for visual representation of the scale. For each scaffold, a single value was assigned to each layer of horizontal pores for a total of three observations per scaffold.

To better understand the reproducibility of the fabrication process, triplicate sets of scaffolds with varying slicing and hatching were created using 900 g/mol PCLTA at 50 wt% with 3 wt % photoinitiator. The scaffold dimensions were measured as described above and variability

between sets at various slicing and hatching distances was reported as the standard error of the mean.

Scale-Up Optimization and Cell Loading Validation

Once the optimal printing parameters, concentration of monomer, concentration of photoinitiator and molecular weight were identified, a prototype of a graft to be used for sub-retinal transplantation in a small animal model was created. This circular scaffold had pore dimensions identical to those described above with an overall diameter of 1 mm and height of 0.1 mm. Samples were prepared, printed and processed as described above, and images were collected using bright field, scanning electron, and confocal microscopy and analyzed as described above. To demonstrate cellular compatibility (i.e., the ability of cells to adhere to and survive within two-photon polymerized PCL scaffolds), clinical-grade human retinal progenitor cells (OTX2+) were generated and seeded onto two-photon polymerized scaffolds as previously described. [44, 45] Cell localization within the scaffolds nine days after seeding was evaluated using nuclear staining, the inherent autofluorescence of PCL, and confocal microscopy (Leica DM 2500 SPE confocal microscope, Leica Microsystems; Wetzlar, Germany).[44, 45]

Retinal Biocompatibility

Prior to transplantation, six two-photon polymerized PCL scaffolds were sterilized by submersion in 100% ethanol for 24 hours, followed by three 30-minute rinses with sterile 1xHBSS. All animal procedures were performed with permission of the University of Iowa IACUC and complied with the ARVO Statement for the Use of Animals in Ophthalmic and Vision Research (https://www.arvo.org/About/policies/statement-for-the-use-of-animals-in-ophthalmic-and-vision-research/). Four-month-old transgenic pigs carrying the human Pro23His mutation in the gene rhodopsin were used as transplant recipients in order to model the ocular dimensions and sub-retinal conditions expected in human retinal degeneration.[46, 47] Each of six animals (two males and four females) underwent sub-retinal transplantation of a 1 x 3 x 0.1 mm two-photon polymerized PCL scaffold (50 wt% PCLTA 900 created using 3 wt% photoinitiator) with vertical and horizontal pores as described above. In the contralateral eye, four animals (two males and two females) received the same surgical treatment with no polymer and two animals (both female) received no treatment. Animals were sacrificed by barbiturate overdose at one-month post-surgery, at which time indirect ophthalmoscopy and spectral-domain OCT (SD-OCT) were performed (Bioptigen Envisu R2200, Bioptogen, Inc., Morrisville, NC). Immediately post-ophthalmoscopic evaluation, eyes were enucleated and fixed in 4% paraformaldehyde overnight, then processed for morphologic analysis. Each animal subsequently underwent a complete necropsy to identify evidence of systemic toxicity and tumorigenicity. Retinal sections were assessed by using paraffin sections stained using hematoxylin and eosin (H&E) and immunohistochemistry and imaged using light and confocal microscopy, respectively. For immunohistochemistry, tissues were treated with anti-recoverin antibody (Millipore, 1:250) to detect photoreceptor cells and DAPI for cell nuclei.

Comprehensive Biocompatibility

To rigorously determine the safety and biocompatibility of photopolymerized PCL, we performed exhaustive testing according to ISO 10993 standards. Due to the high volume of samples required for this testing, we created samples for these assays using UV photopolymerization (see Supplemental Information). As per the samples used in the retinal biocompatability study described above, scaffolds were extensively rinsed with 1,4-dioxane and balanced salt solution prior to sterilization (see Supplemental Information). Assays were performed according to ISO 10993 standards by an independent testing service (WuXi AppTec, St. Paul, MN). Briefly, for cytotoxicity analysis PCL scaffold extracts (obtained over 72hrs in E-MEM with 5% FBS) were feed to L-929 mouse fibroblast cells, which were evaluated at 24, 48, and 72 hours post-feeding. To evaluate genotoxicity, two independent assays, 1) an *in vitro* mouse lymphoma assay and 2) a bacterial mutagenicity assay, were performed. To test pryogenicity, PCL scaffold extracts were injected into rabbits and febrile responses were measured. To determine if photopolymerized PCL scaffolds have the ability to activate the immune system and stimulate an allergic response, a guinea pig sensitization assay was performed. To determine if photopolymerized PCL elicits any subacute toxicity or acute systemic toxicity, three independent mouse injection studies were performed. In Study 1, animals received IV extract injections and were evaluated over a 14 day time period (subacute toxicity). In Study 2, animals received intraperitoneal (IP) extract injections and were evaluated over a 14 day time period (subacute toxicity). Finally, Study 3 consisted of animals that received a single IP or intravenous (IV) injection of PCL extract and were evaluated at 72 hours (acute toxicity).

Extracts from photopolymerized PCL samples were also analyzed by gas chromatography-mass spectrometry to identify volatile to semi-volatile compounds, liquid chromatography-mass spectrometry to identify semi-volatile to non-volatile compounds, inductively coupled plasma mass spectrometry to identify elemental (metal and other) components and headspace gas chromatography-mass spectrometry to identify residual solvents and other volatile components. All compounds identified were subsequently evaluated for potential toxicity via worst-case exposure (i.e., effect of 100% daily bioavailability), based on their concentrations identified in the extract (HDE). Levels of each compound that could be tolerated (TI) were derived from existing regulatory values, toxicity data, and *in silico* prediction, and a margin of safety value was subsequently calculated. Margin of safety (MOS) values of greater or equal to 1 (where MOS = TI / HDE), were considered safe.

Statistical Analyses

Three-way analysis of variance—Three-way ANOVA was used to assess the relative contributions of three variables (polymer concentration, polymer molecular weight and slicing or hatching distance) on scaffold width and height as well as pore roundness and diameter. The limitations of the test required reducing the number of levels for each variable to two. For molecular weight, no more than two levels (300 g/mol and 900 g/mol) had been selected for the experiment, so all levels were included. For slicing and hatching, only the upper and lower bounds of the experimental range (0.1 μm and 0.5 μm) were selected for three-way ANOVA. Since the use of 900 g/mol PCLTA at 75 wt% resulted in poor or no printing and thus data could not be collected from this group, 25 wt% and 50 wt% were

selected as the levels of interest for polymer concentration. Three-way ANOVA also demands an equal number of replicates for each sample, yet some scaffolds were incomplete and did not have as many pores as designed. Thus, for pore diameter and roundness, we only included the first three measurements for each sample in our analysis. A few scaffolds were void of pores altogether, in which case zeros were used as the measurement of pore diameter and roundness. Data were assumed to be normally distributed and were assessed at a confidence interval of 95%. For each measured outcome, the percentage of variation attributed to each variable or interaction was reported as a pie chart.

Two-way analysis of variance—For each measured outcome, the two variables that contributed most to measurement variation (either alone or in interactions) were further analyzed via two-way ANOVA. For molecular weight, the levels were 300 g/mol and 900 g/mol. For slicing and hatching, levels were 0.1 μm, 0.5 μm, 1.0 μm and 1.5 μm. For polymer concentration, the experimental levels used for two-way ANOVA were 25 wt% and 50 wt% (as no data could be collected for 900 g/mol PCLTA at 75 wt%). Data were assumed to be normally distributed and were assessed at a confidence level of 95%. Where relevant, post-hoc Tukey's multiple comparisons tests were performed for slicing or hatching distance, while Sidak's multiple comparisons tests were performed for molecular weight and polymer concentration, each at a confidence level of 95%.

One-way analysis of variance—In the instance that polymer concentration was identified by three-way ANOVA as contributing strongly to variance, one-way ANOVA and Tukey's multiple comparisons tests were performed for 300 g/mol PCLTA only with 25 wt %, 50 wt%, and 75 wt% in addition to the two-way ANOVA described above that excluded 75 wt%. Data were assumed to be normally distributed and were assessed at a confidence interval of 95%.

Results

Determination of printing thresholds

As expected, the laser power required to induce a two-photon polymerization event increased with increasing scanning speed (Figure 2). For both PCLDA and PCLTA, increasing molecular weight also slightly increased the laser power required for polymerization (Figure 2A). In fact, the largest molecular weight prepolymer we created for this study (PCLDA 2000) did not polymerize within the bounds of our experiment (at or above 6 mm/s with 100% laser power). However, for those PCLDA prepolymers that did polymerize, increasing molecular weight also increased the range of laser powers at which the structures resembled the model (Figure 2B). At all scanning speeds and regardless of molecular weight, polymerization of PCLDA required much higher laser power compared to PCLTA and simply did not polymerize at scanning speeds greater than 40 mm/s (Figure 2A). In addition, unlike PCLTA structures, most PCLDA structures did not resemble the modeled star or lacked intricate details such as star points (Figure 2B). Due to this poor polymerization, only the PCLTAs were considered for the remaining experiments.

Photoinitiator concentration did not cause clear differences in the minimum laser power required for polymerization (Figure 2C). However, qualitatively, crosslinked PCL structures

formed with 1 wt% photoinitiator were larger and had fewer sharp edges than those formed with 3 or 5 wt% (Figure 2D). Thus, to conserve resources while maintaining optimal structure quality, 3 wt% was selected as the photoinitiator concentration for successive experiments. At scanning speeds below 40 mm/s, the prepolymer concentration did not appear to affect polymerization threshold (Figure 2E). At scanning speeds above 40 mm/s, the 25 wt% formulations required higher laser power to polymerize than 50 wt% or 75 wt%. Although there were some scanning speeds at which 75 wt% PCLTA 300 required a higher laser power than 50 wt%, these differences were inconsistent across all scanning speeds. Furthermore, at a given scanning speed, the range of laser powers that resulted in structures that resembled the model was larger for 25 wt% PCLTA 300 than for 50 wt% or 75 wt% (Figure 2F). Similar results were noted for PCLTA 900 (data not shown). Taken together, these results indicated that polymer concentration may play a role in fidelity of structure to the model and that each formulation would require its own optimized scanning speed and laser power in order to achieve the best two-photon resolution.

Determination of print resolution

Regardless of polymer formulation, the use of high laser scanning speeds led to imprecise printing of the edges of two-photon polymerized structures (Figure 3A). We aimed to avoid these aberrant features while also creating high-resolution tissue scaffolds within a feasible timeframe. Thus, we selected the fastest laser scanning speed that did not cause this artifact (Table 1) and characterized resolution at that scanning speed to select optimal polymerization conditions. For each formulation, the star width at the polymerization threshold was smaller than the modeled width (Figure 3B–C). This width increased with increasing laser power, except in the case of 75 wt% PCLTA 900, which at the selected scanning speed produced stars smaller than the modeled star regardless of laser power (Figure 3C). 50 wt% and 75 wt% PCLTA 300 were characterized at the same scanning speed (40 mm/s), as were 25 wt% and 50 wt% PCLTA 900 (60 mm/s). Thus, these resolution trends can be compared directly to infer the influence of polymer concentration on feature width. For PCLTA 300, increasing the polymer concentration increased the laser power necessary to achieve star widths similar to the modeled width, while the overall width per laser power ratio (slope) appeared to be independent of polymer concentration (Figure 3B). Conversely, the width of structures created with 25 wt% or 50 wt% PCLTA 900 did not appear to be influenced by polymer concentration (Figure 3C). For each formulation, the laser power that resulted in a mean point-to-point distance closest to the design (~9.5 μm) was chosen as the optimal laser power for future two-photon polymerization experiments (Table 1).

Analysis of Model to Scaffold Fidelity

Scaffold Width—With a constant hatching distance, the slicing distance and molecular weight, as well as their interactions with each other and with prepolymer concentration, were statistically significant ($p < 0.0001$) contributors to variability in scaffold width (Table S1A). Prepolymer concentration alone was the only non-significant variable ($p = 0.8493$). Specifically, the variables that contributed most to the width of structures were molecular weight and slicing distance, which caused 33% and 34% of the total variation, respectively (Figure 4A). Narrowing the analysis using the average across all polymer concentrations

reinforced the significance of slicing distance and molecular weight ($p < 0.0001$) rather than their interaction (Table S1B). In general, increasing slicing distance or increasing molecular weight decreased scaffold width, meaning that the structures were more dissimilar to the model (Figure 4A–B). Regardless of molecular weight, using a slicing distance of 1.0 or 1.5 μm resulted in scaffolds with significantly smaller widths ($p < 0.05$) than scaffolds created using a slicing distance of 0.1 μm (Table S1C). Furthermore, the difference in scaffold width between 300 and 900 g/mol was significant ($p < 0.05$) for all slicing distances except 0.5 μm (Table S1D).

When slicing distance was held constant, trends in scaffold width were similar to those observed when hatching distance was constant. Although all variables and their interactions played significant roles in scaffold width ($p < 0.0001$, Table S1E), the greatest contributors to variation were hatching distance (39%) and molecular weight (39%) (Figure 4C). In a subsequent consolidated analysis examining only hatching distance and molecular weight, both factors and their interaction were significant ($p < 0.05$). However, the factors contributed more independently to the variation than their interaction (26% and 44% for hatching distance and molecular weight, respectively, compared to 5% for their interaction) (Table S1F). In general, increasing hatching distance or molecular weight decreased scaffold width (Figure 4C), thus causing a decrease in the extent to which the scaffold resembled the model. For a molecular weight of 300 g/mol, the only significant difference in scaffold width was between 0.1 and 1.5 μm ($p < 0.01$). The effect of hatching distance was more pronounced for 900 g/mol: using a hatching distance of 0.1 μm resulted in significantly wider scaffolds than using a hatching distance of 1.0 or 1.5 μm ($p < 0.01$, Table S1G). Furthermore, using a hatching distance of 0.5 μm resulted in a significantly larger scaffold width than the use of 1.5 μm ($p < 0.001$, Table S1G). Conversely, the use of 300 g/mol PCLTA resulted in significantly wider scaffolds than 900 g/mol PCLTA at every hatching distance ($p < 0.01$, Table S1H).

Vertical Pore Diameter—At a constant hatching distance, the interaction between molecular weight and concentration of prepolymer had the largest effect of the experimental variables on scaffold vertical pore diameter, contributing 62% of the total variation (Figure 5A–B and Table S2A–B). At 25 wt% polymer, the pores of scaffolds created using 300 g/mol PCLTA were significantly larger (i.e., closer to the modeled diameter) than the pores of scaffolds created using 900 g/mol PCLTA, while at 50 wt% the 900 g/mol pores were larger than their low molecular weight counterparts ($p < 0.0001$, Table S2C). In fact, the pore size of 900 g/mol PCLTA scaffolds increased significantly when prepolymer concentration increased from 25 to 50 wt% ($p < 0.0001$, Table S2D). Conversely, the diameter of 300 g/mol PCLTA scaffold pores decreased significantly as concentration increased from 25 to 50 wt%, then increased again when the concentration was further increased to 75 wt% (both $p < 0.0001$, Table S2D–E). The 75 wt% 900 g/mol PCLTA consistently over-polymerized, filling the pores and solidifying all printed structures into a block (data not shown).

Similarly, at constant slicing distance, the interaction between molecular weight and prepolymer concentration contributed the most to variations in scaffold vertical pore diameter (52% of total, Figure 5C and Table S2F–G). As in the constant hatching

experiment, increasing molecular weight decreased pore diameter at 25 wt% but increased pore diameter at 50 wt% (both $p < 0.0001$, Table S2H). Likewise, increasing polymer concentration from 25 to 50 wt% increased pore diameter for 900 g/mol PCLTA ($p < 0.0001$, Table S2I). On the other hand, for 300 g/mol PCLTA, scaffold pore diameter decreased as polymer concentration increased from 25 to 50 wt%, but increased again between 50 and 75 wt% ($p < 0.0001$, Table S2I–J). Consistent with the hatching experiments, the 75 wt% 900 g/mol PCLTA over-polymerized and thus was omitted from these results.

Scaffold Height—Overall, slicing distance (55% of variation) and, to a lesser extent, molecular weight (12% of variation) dictated scaffold height at a constant hatching distance (Figure S4A–B and Table S3A–B). In general, scaffold height decreased with increasing slicing distance or molecular weight. Specifically, 300 g/mol PCLTA scaffolds created using a slicing distance of 1.5 μm were significantly shorter than those created using a slicing distance of 0.1 or 0.5 μm (both $p < 0.05$, Table S3C). This effect was even more pronounced in 900 g/mol samples: scaffolds created using a slicing distance of 1.5 μm were significantly shorter than those created with slicing distances of 0.1, 0.5, or 1.0 μm ($p < 0.0001$, $p < 0.0001$ and $p < 0.001$, respectively, Table S3C). Meanwhile, scaffolds created using 900 g/mol PCLTA were only significantly shorter than those composed of 300 g/mol PCLTA at a slicing distance of 1.5 μm ($p < 0.0001$, Table S3D).

When slicing distance was held constant, prepolymer concentration contributed the most to variations in scaffold height (45%) followed by an interaction between all of the factors (16%, Figure S4C, Table S3E). When scaffold heights were averaged across both molecular weights (Table S3F), overall their values decreased with increasing hatching distance and were maximal at a prepolymer concentration of 50 wt%. In fact, 50 wt% and 75 wt% scaffolds were significantly taller when created using a hatching distance of 0.1 μm compared to 1.0 or 1.5 μm hatching distances ($p < 0.05$ and $p < 0.01$, respectively, Table S3G). Differences in the height of scaffolds created using 25 wt% versus 75 wt% prepolymer were not significant at any hatching distance (Table S3H). Conversely, the use of 50 wt% prepolymer resulted in significantly taller scaffolds than those composed of either 25 wt% or 75 wt% at each hatching distance (Table S3H).

Vertical Pore Roundness—The two largest contributing factors to vertical pore roundness at constant hatching distance were the interaction between molecular weight and prepolymer concentration (38%) and the interaction between slicing distance and prepolymer concentration (21%, Figure S5A–B and Table S4A). It should be noted that in this instance, averaging across all slicing distances and removing 75 wt% from the analysis (due to incomplete data), inflated the influence of polymer concentration and de-emphasized the importance of the interaction between molecular weight and prepolymer concentration (Table S4B). Nonetheless, under these circumstances, pores were significantly more round when scaffolds were created using 300 g/mol versus 900 g/mol PCLTA at 25 wt%, but the opposite occurred at 50 wt% ($p < 0.001$ and $p < 0.05$, respectively, Table S4C). For either molecular weight, pore roundness significantly decreased when prepolymer concentration increased from 25 wt% to 50 wt% (both $p < 0.0001$, Table S4D), but increasing the prepolymer concentration from 50 to 75 wt% (data only available for 300 g/mol PCLTA)

resulted in a subsequent increase in pore roundness, though this value was still significantly smaller than the roundness at 25 wt% (all $p < 0.0001$, Table S4E).

Prepolymer concentration had the greatest impact on pore roundness at a constant slicing distance (42% of variation), followed by the interaction between all of the variables (15%, Figure S5C and Table S4F–G). Increasing molecular weight significantly decreased pore roundness ($p < 0.0001$), but only with the use of 25 wt% prepolymer (Table S4H). Furthermore, similar to the results described above for constant hatching distance, pore roundness significantly decreased when prepolymer concentration increased from 25 wt% to 50 wt% (both $p < 0.0001$, Table S4I), but increasing the prepolymer concentration from 50 wt% to 75 wt% resulted in a subsequent increase in pore roundness, though this value was still significantly smaller than the roundness at 25 wt% (all $p < 0.0001$, Table S4J).

Horizontal Pore Quality—At a constant hatching distance, horizontal pore quality depended most on prepolymer concentration (mean difference of 1.25 versus 0.75 for either slicing distance or molecular weight, Table S5A). Overall, maximal pore quality occurred in samples created using a prepolymer concentration of 50 wt% (Figure S6A–B). Increasing molecular weight qualitatively increased horizontal pore integrity, while the effect of increasing slicing distance was less distinct (Figure S6A–B). Similarly, prepolymer concentration contributed the most to horizontal pore quality (46%) at a constant slicing distance (Table S5B). As in the experiment where hatching distance was held constant, in general maximal pore quality was achieved through the use of 50 wt% 900 g/mol PCLTA (Figure S6C).

Reproducibility—At a constant formulation (i.e. prepolymer concentration and molecular weight) and hatching distance, increasing the slicing distance did not noticeably reduce the deviance of vertical pore diameter or roundness from the design values (Figure S7A). Conversely, scaffold width became more variable as slicing distance increased, while scaffold height deviance initially decreased, then sharply increased with increasing slicing distance (Figure S7A). The variability of scaffold features due to hatching distance was overall smaller than the variability caused by varying slicing distance (Figure S7B). In fact, all standard errors of the mean appeared to be independent of hatching distance and were less than 10%, except for the variability of scaffold width at a hatching distance of 1.5 μm.

Scale-Up Optimization

To feasibly treat an area of tissue with scaffold-assisted cell therapy, an implant with tissue-relevant overall dimensions is necessary. Specifically, as patients who retain even just the central 1mm of their retina may have very useful vision, the goal was to be able to print scaffolds that are a minimum of 1mm in diameter, preferably larger. Fabrication of a continuous two-photon polymerized structure using the instrument we describe here is limited to an area roughly 250 μm x 250 μm in size. Structures larger than this may be constructed as a series of segments that are “stitched” together by slightly overlapping the laser path and thus covalently linking each segment to its neighbors. Thus, the effect of the described variables on scaffold width determined, to some extent, their contributions to scale-up success or failure. For example, we initially selected formulation variables that

were expected to result in scaffolds with maximal width and acceptable height and vertical pore dimensions (75 wt% 300 g/mol PCLTA), but chose the highest slicing and hatching distances (each 1.5 μm) in order to minimize fabrication time of a 1 mm diameter scaffold. Although the resulting scaled-up scaffold took only one hour to create, it lacked essential structural integrity in the stitches between segments (Figure 6A) and did not withstand even gentle handling. Decreasing both slicing and hatching distance to 1.0 μm increased the fabrication time to seven hours, while significantly improving structural integrity (Figure 6B) and mechanical robustness.

Higher magnification methods, namely SEM and Confocal microscopy, were pursued to validate structural accuracy and fidelity of the scaled up scaffold. As shown in Figure 6C **and** D, the scaffold to model fidelity, as indicated by adherence of the vertical pores to the original model, was maintained. Specifically, the diameter and roundness of the vertical pores in this scaled-up scaffold are 15.9 ± 4.07 μm and 0.866 ±0.0889, respectively, which is consistent with the preliminary, single print area scaffold outcomes. Likewise, pores were free of excess polymer and the stitching edges remained intact (i.e. Figure 6D arrows, flat surface between vertical pores created during the stitching process, which is essential for structural integrity of the scaled-up scaffold), indicating that this scaled-up scaffold was structurally conserved during post-fabrication processing. To demonstrate compatibility of the scaffold with living cells, human iPSC-derived OTX2-positive retinal progenitor cells (Figure 6F) were generated using our previously published cGMP retinal differentiation protocol [45] and seeded within scaled-up 1mm scaffolds (Figure 6E, G **&** H). Nine days after seeding, grafts were harvested, fixed and stained using the nuclear marker DAPI. As shown in Figures 6G **&** H (**G** – top down surface view taken to show maintenance of cells within each of the printed pores, **H** – tilted view taken to show cells at different heights seeded down through each pore one above the other as is the case in the normal human retina), human iPSC derived retinal progenitor cells were maintained within each of the pores, where they are largely protected from the shear forces that would normally be encountered during subretinal transplantation surgery. The fact that these cells could be maintained within these scaled-up PCL scaffolds for up to 9 days post-seeding indicates a lack of acute toxicity from residual un-polymerized monomer and/or washing reagents.

Retinal Biocompatibility

As indicated above, the desired purpose of this work was to not only fabricate a highly intricate and degradable tissue scaffold at human-relevant size scales, but also to demonstrate the biocompatibility of such a material. For this analysis, rectangular scaffolds were designed with the same porous structure as the generic scaffolds described above and printed at the maximum size (1 x 3 x 0.1 mm) that could be readily placed beneath the retina surgically using custom-developed instrumentation. One month after transplantation of these scaffolds into the sub-retinal space of transgenic retinal degenerative Pro23His rhodopsin mutant pigs (i.e., a model of autosomal dominant retinitis pigmentosa),[46] no evidence of uveitis (i.e., intraocular inflammation) was detected on ophthalmoscopic examination and most retinas spontaneously re-attached (Table S6). Using optical coherence tomography, the scaffolds were imaged and observed to be lying flat in the correct location within the sub-retinal space (Figure 7A–B). Postmortem histological observation demonstrated that some

host cells had migrated into the scaffold (Figure 7C–F). In addition, recoverin-labeled photoreceptor cells were maintained both above and inside the vertical pores of the auto-fluorescent PCLTA scaffold (Figure 7E–F). Compared to the control (Figure S8), no evidence of toxicity to adjacent photoreceptor cells and/or inner retinal neurons was detected (Figure 7C–F, Figure S9). Finally, following gross necropsy, there was no evidence of tumor formation or tissue necrosis to suggest abnormal cellular proliferation or systemic toxicity in any of the tissues listed in Table S7.

Comprehensive Biocompatibility (ISO 10993) Testing

Cytotoxicity, genotoxicity, pyrogenicity, sensitization, subacute toxicity, and systemic toxicity of photopolymerized PCL were assessed using ISO 10993 testing under good laboratory practices (Table 2). In the cytotoxicity assay, no evidence of increased toxicity above the negative control was reported. Likewise, genotoxicity, as evaluated by two independent experiments (Mouse Lymphoma and Bacterial Mutagenicity), was negative. To test pyrogenicity PCL scaffold extracts were injected into rabbits and febrile responses were measured. No evidence of extract induced fever was detected in either of the 3 animals tested. Likewise, sensitization studies did not produce adverse clinical events in any animal and importantly, none of the test animals challenged with PCL scaffold extracts were observed to have a sensitization response above control. In the sub-acute and systemic toxicity studies, all animals in both test and control groups survived for the duration of their respective studies and no significant clinical adverse events were detected in any animal. In addition, no mean body weight changes, significant findings at necropsy, significant pathology or hematologic findings that would indicate scaffold induced-toxicity were identified.

The likelihood that degraded components of photopolymerized PCL scaffolds, identified following exhaustive extraction under exaggerated conditions, could pose an unacceptable risk to patients was also assessed (Table 3). Of all components identified, trimethylolpropane monoacrylate was the only compound that was predicted to have a margin of safety less than 1 for 100% delivery at 24 hours. However, if 100% was delivered over a 30 day span, which is still significantly faster than that predicted for PCL, this value was greater than one, indicating minimal risk.

Discussion

Scientific and commercial interest in two-photon lithography has steadily grown since its inception more than twenty years ago. To date, however, its use for studying or treating human disease has been limited by the unavailability of suitable technologically and biologically compatible prepolymers. Poly(caprolactone), a component of several FDA-approved devices, is well-characterized in the literature, and its physical properties can be easily manipulated, as discussed above. In this study, we used photo-curable multi-acrylated PCL to demonstrate how biologically relevant polymers in general can be optimized for use in two-photon polymerization systems. Through extensive testing to define optimal printing parameters, we further demonstrate that two-photon polymerization as a method of creating

high-quality 3D structures depends on several factors, including prepolymer functionality, molecular weight, and concentration.

Our results indicate that PCLDA requires a higher laser power to undergo two-photon polymerization than PCLTA (Figure 2). Indeed, PCLDA is known to react more slowly during photopolymerization than PCLTA, as demonstrated in a recent study from our group.[26] These kinetic differences can likely be attributed to differences in reactive group concentration, since PCLDA has fewer acrylate groups per molecule than PCLTA and thus fewer reactive sites available for crosslink formation. Likewise, prepolymers with a greater concentration of reactive groups (e.g., PCLTA), also form more highly cross-linked structures (i.e., reach a higher conversion) upon polymerization than their low functionality counterparts (e.g., PCLDA).[26] This too is consistent with our results, as integrity to the model was conserved during two-photon polymerization of PCLTA stars, but not of PCLDA. A similar trend was observed in scaffold fabrication: increasing the concentration of reactive groups, either by selecting a prepolymer with a lower molecular weight or by increasing prepolymer concentration, increased the fidelity of the scaffold to the model. For example, vertical pore diameter generally increased towards the modeled diameter as prepolymer concentration increased (Figure 5). As an exception, structures fabricated using 25 wt% PCLTA 300 had vertical pore diameters larger than those fabricated with 50 wt% of the same prepolymer. This discrepancy is likely a result of the more rapid solvent evaporation that occurred in these specimens, which artificially increased prepolymer concentration in an uncontrolled manner. Although the differences were slight, increasing molecular weight also increased the laser exposure needed to achieve a two-photon polymerization event. In fact, the highest molecular weight prepolymer we studied (PCLDA 2000) did not polymerize at even the slowest scanning speeds and highest intensity laser exposures. The effect of molecular weight also extended to larger structures; decreasing molecular weight increased scaffold width (Figure 4) and vertical pore diameter (Figure 5), each of which represent improved accuracy to the model. This phenomenon can likewise be attributed to reactive group concentration and its related effect on photopolymerization kinetics.[26] Despite the apparent importance of maximizing reactive group concentration for optimum two-photon polymerization behavior (i.e., fidelity to the model), there also seems to be a limit to this effect. In particular, we observed substantial and consistent over-polymerization of scaffolds fabricated using 75 wt% PCLTA 900. This behavior is likely due to the Trommsdorff Effect; at high concentrations, some monomers (or prepolymers) reach a viscosity (a.k.a the gel point) at which activated free radicals become diffusion-limited.[48] Thus, termination decreases (since radical recombination is inhibited), causing an increase in polymerization rate potentially extending the longevity of the reaction after light exposure ceases. Since PCLTA 900 can is anticipated to undergo the most chain entanglement of all the prepolymers investigated, this phenomenon is feasible given the relatively high concentration (75 wt%) used for these particular samples. Moreover, this observation highlights the ongoing importance of understanding two-photon polymerization kinetics and the balance required in selecting appropriate prepolymers for its use in biomedical applications.

The extent to which two-photon polymerized scaffolds match the 3D model is important not only for reliability and reproducibility of a material, but also for proper function and scale-

up. Based on our preliminary studies, we hypothesized that minimizing structure shrinkage was critical to achieving successful scale-up. Creating larger, translationally relevant scaffolds requires “stitching” of smaller segments. If the width of each segment is too small, these pieces will not form proper connections with one another. Thus, according to our measurements of scaffold width, we selected 300 g/mol PCLTA for our scale-up studies, as it produced structures that were closer to the 3D design than 900 g/mol PCLTA (Figure 4). Vertical pores, designed to hold stem cell derived photoreceptor cells in a pseudostratified epithelium as in the retinal outer nuclear layer, are the most important functional feature of our proposed scaffolds. Although the dimensions of the pores can easily be tuned by adjusting the 3D model, adherence to the model without a need for retrospective adjustment is strongly preferred. Thus, we chose to use a prepolymer concentration of 75 wt%, which resulted in the least amount of pore shrinkage (Figure 5). Although our data also indicated that the use of small slicing and hatching distances would result in the least deviant structures, fabrication time is a major concern for the adoption and scale-up of two-photon polymerization in biotechnology. We were able to balance these two factors during scale-up by selecting slicing and hatching distances that resulted in larger scaffolds with excellent integrity and reasonable production time (Figure 6).

Ideally, scaffold degradation would occur at a rate similar to the rate of deposition of natural extracellular matrix during donor cell maturation *in vivo*. In such a case, the support provided by the scaffold would gradually be replaced by native retinal biomolecules such that cellular alignment and structural integrity of the tissue would persist indefinitely after scaffold dissolution. While it is not yet clear how quickly these natural structural replacement processes will occur and therefore what the optimal degradation rate will be for photoreceptor scaffolds, previous studies suggest that the rapid degradation of PLGA and PLA results in acidic accumulation and local toxicity while PCL does not, due to its slower hydrolysis.[26, 49] The majority of *in vivo* PCL degradation studies to date have been performed using sub-cutaneous implantation of linear PCL biomaterials. Thus, the fraction of polymer remaining after approximately one month varies between studies, with reported values of 60% (solvent-cast and salt-leached sample with starting M_w = 114,000),[49] 84% (electrospun sample with starting M_w = 85,300),[20] and 92% (solvent-cast capsule with starting M_w = 305,000).[24] The degradation kinetics of photopolymerized PCL samples are not as well-characterized, and have never been investigated *in vivo*. However, given that photopolymerization in the context described here introduces additional covalent bonds that are not readily hydrolyzed, and a network architecture with little room for water invasion, degradation rates are expected to be slower for these materials than for linear PCL materials, even those with high starting molecular weights. Indeed, after one month, non-porous photopolymerized PCL retains 97 - 99% of its original mass when degraded *in vitro*, and the extent of hydrolysis depends on the crosslinking density of the sample.[26] Assuming similar backbone chemistry, increasing prepolymer molecular weight or decreasing functionality will cause a concomitant decrease in crosslinking density and would be expected to increase the degradation rate of photopolymerized PCL. This hypothesis is supported by published data from the same study, where under accelerated conditions, photopolymerized PCLTA 300 took nearly three times longer to completely degrade than PCLDA 1250.[26] Although extrapolation of degradation trends is often not accurate given

the high degree of non-linearity of such processes, extension of these published degradation data for the purposes of estimation indicate that degradation time under non-accelerated *in vitro* conditions is expected to be several years or more. Thus, we are confident that PCL's slow degradation, especially crosslinked PCLTA 300, will allow acidic molecules to be neutralized and cleared before damage to the retinal tissue occurs.

Several groups, including our own, have transplanted photoreceptor cell-laden scaffolds in animal retinas in an effort to assess their safety and efficacy. However, even when using an animal whose ocular anatomy is strikingly similar to the human, such as the pig, there are major limitations to this endeavor. The treatment approach we intend to use for ameliorating late-stage retinal degeneration involves patient-specific iPSC-derived photoreceptor cells. Thus, to precisely recapitulate and assess this approach in an animal would necessitate generating "patient"-specific photoreceptor cells for each animal. This activity would thus require an astronomical financial and temporal cost, and there would still be no guarantee that the results (positive or negative) would accurately reflect the expected response of human tissue. As an alternative, scaffolds laden with human photoreceptor cells could be transplanted in a porcine model. However, this approach would result in immediate immune rejection of the implant and premature death unless immune suppressants were administered. Yet, using such drugs precludes the ability to determine whether the scaffold itself is acutely toxic (locally or systemically), since inflammatory mechanisms would, by definition, be inhibited.

On the other hand, exhaustive toxicity assessed *in vitro* is generally a poor representation of compatibility *in vivo*. For example, mechanical forces, immune reactivity, and interactions with multiple cell types (in this case, the INL and the RPE), which are all critical to implant success, are absent *in vitro*. Regardless, optimization of the interaction between replacement photoreceptor cells and degradable scaffolds is certainly important. While two-photon polymerized scaffolds have been shown to facilitate photoreceptor cell alignment[44] and photopolymerized PCL has been shown to support the attachment of human iPSCs,[26] there are many additional factors at play, which should be addressed using a more thorough *in vitro* model of the retina. The best-constructed *in vitro* model would rely on the same strategy that we are actively pursuing for clinical use. That is, human iPSCs can be differentiated towards a photoreceptor cell lineage using the current gold standard approach that relies on three-dimensional differentiation.[45, 51–55] In order to yield photoreceptor precursor cells, these protocols require careful and costly culture techniques for long periods of time, all for a relatively low yield (i.e., very few of the resulting cells are photoreceptor precursors). More importantly, true characterization and optimization of the interactions between these human photoreceptor precursor cells and our two-photon polymerized scaffolds will require consideration of differentiation timeline before scaffold seeding, cell seeding density, co-culture with human IPSC-derived RPE or cells of the inner nuclear layer, time of culture for proper cell alignment and maturation, survival of the cells after surgical manipulation, and so on. In other words, our ultimate goal is to create a well-constructed *in vitro* model of the retina, and such experiments are ongoing. However, as such an endeavor constitutes a sizeable body of work that is outside the scope of the current manuscript, we elected to focus on the biocompatibility of the scaffolds and their degradation products alone by delivering them without cells and rigorously assessing tolerability.

We have previously shown that two-photon polymerization can be used to create scaffolds using commercially available, non-degradable photoresists that encourage vertical orientation of retinal progenitor cells.[44] In this study, we have presented promising results to suggest that two photon polymerized PCL based photoreceptor cell delivery scaffolds are compatible with the degenerative host retina (Figure 7). Specifically, at 1-month following subretinal transplantation of scaled photoreceptor cell delivery scaffolds in the non-immune suppressed Pro23His rhodopsin mutant retinal degeneration pig, no sign of scaffold-inflicted retinal injury, inflammation, systemic toxicity, or tumor formation was detected. Some migration of host cells into the scaffold was observed. These cells seem to be a combination of photoreceptor and RPE cells based on their expression of recoverin and melanin pigment respectively. Such migration is not expected under clinical conditions, since in a true transplant situation the vertical pores will be filled with human iPSC derived retinal cells, offering little room for endogenous cells to migrate into the scaffold. However, the local cellular response to the material in question is important to consider. Transplantation of any polymeric material is bound to disrupt retinal structure to a certain extent. Intraretinal RPE migration is one type of injury response in the form of proliferative vitreoretinopathy, which can occur in some forms of retinal degeneration. This adverse clinical outcome is the result of RPE junctional complex loss and can eventually cause retinal fibrosis and detachment. Since full characterization of migrated cells was outside the scope of this study, there is no guarantee that the cellular displacement observed was not a pathological consequence of polymer transplantation. Nevertheless, the presumed RPE cell migration was limited both in number of cells and in distance traveled. Definitive claims about this process as a response to polymer transplantation cannot be made without additional experimentation. While cell migration into the scaffold in this study suggests that the material has not been encapsulated by fibrous matter, the local cellular response should be closely monitored in future studies to ensure that cells, particularly the RPE, do not transition toward an undesirable phenotype (e.g., an epithelial to mesenchymal transition).

The fact that the Pro23His rhodopsin pig has a retinal degenerative disease akin to patients with retinitis pigmentosa and that its eye is anatomically similar to human, supports the translatability of the reported surgical approach and scaffold for human cell replacement strategies. While the thickness of the sample and the size and spacing of vertical and horizontal pores were consistent with scaffolds we expect to use in the future in humans, there are some macroscopic design differences. Specifically, we believe a circular sample with a diameter of 5 mm to be appropriately sized for the human retina, while here we used a 1 mm x 3 mm rectangular scaffold (which was chosen due to availability of subretinal surgical delivery device). We hypothesize that circular samples would be biomechanically compatible than their rectangular counterparts, since stress localization at edges and corners would be minimized or eliminated, respectively. That said, there is a possibility that scaffold size will contribute to differences in biocompatibility based on biomechanics, since a larger sample may be less likely to conform to the curvature of the eye and thus may be more likely to cause a retinal detachment. If such a finding was identified, reversion to the 1 mm x 3 mm strips used in this study, which are more similar in size to those used in ongoing clinical trials for subretinal delivery of RPE, could be used.

On the other hand, any concerns about biochemically-driven differences in biocompatibility related to scale (e.g., due to accumulation of degradation products) are addressed by the regulatory-grade biocompatilbity ISO 10993 tests presented, which were performed using specimens with equivalent surface area to 5 mm circular samples. In brief, the overall toxilogical risk associated with photopolymerized PCL scaffolds was determined to be low based on these extensive studies (Tables 2–3). Due to the high volume of samples needed for such extensive testing, there was a minor chemical difference between two photon polymerized samples and those used for ISO 10993 testing. Specifically, the larger ISO 10993 specimens were created using UV photopolymerization (see Supplemental Materials and Methods), which necessitated using a different photoinitiator than their two-photon polymerized counterparts. The photoinitiator used for ISO 10993 testing (colloquially known as Irgacure 2959), undergoes efficient initiation in the UV range (with peak extinction ~275 nm) and is more water soluble than other commonly-used photoinitiators. Thus, its minimal toxological effects have been relatively well-characterized since it is an appealing choice for many biomedical applications. However, it does not cause polymerization via two-photon initiation when exposed to a 780 nm light source. Conversely, the photoinitiator used in the majority of this study (informally known as Irgacure 369), is able to undergo two-photon initiation at this wavelength, but it is not water soluble and its traditional (i.e., single photon) initiation occurs at higher wavelengths (peak extinction ~320 nm) than Irgacure 2959. Since Irgacure 369 is not compatible with hydrogel systems and is more susceptible to spontaneous initiation by visible light than other photoinitiators, it is not as popular a choice for academic photopolymerization systems, particularly in the biomedical sciences, and its biological repurcussions are not as well understood. Although it is possible that Irgacure 369 presents hazards that Irgacure 2959 does not, these will likely be dose-dependent. Furthermore, as Irgacure 2959 was not identified as a product of exhaustive extraction (i.e., total device dissolution) during ISO 10993 testing, nor were its derivatives, we assume that the vast majority of photoinitiator was consumed during reaction or removed during the rinsing process. Given the absence of adverse local or systemic outcomes after sub-retinal transplantation of two-photon polymerized PCL scaffolds generated using Irgacure 369, we expect that the same will be true. That said, prior to moving this technology into the clinic, complete extraction of two-photon polymerized PCL scaffolds and analysis of extraction produts in comparison to their photopolymerized ISO 10993 tested counterparts should be performed.

There are many additional factors to consider before clinical trial in humans, many of which we have discussed above. However, the results presented here signify a critical juncture towards more effective transplantation strategies for those suffering from late-stage retinal degeneration. Moreover, as the method we describe can be adapted to a wide range of polymer chemistries, our results can be utilized for a variety of different biomedical applications beyond photoreceptor cell replacement. Given that microstructural control of degradable polymers has historically been a limitation for many applications, this work represents a significant step forward in the field of precision biomaterials.

Supplementary Material

Refer to Web version on PubMed Central for supplementary material.

Acknowledgments

The authors gratefully acknowledge internal sample preparation by Arwin Shrestha, Rion J. Wendland, Abigail R. Krueger, and Stephon D. Berry; external experimental services by WuXi AppTec; and financial support from the National Institute of Health [R01 024605-01, & P30 EY025580], Research to Prevent Blindness (RPB) and the International Retinal Research Foundation (IRRF) (Catalyst Award), Fight for Sight (postdoctoral fellowship), the Howard F. Ruby Endowment for Human Retinal Engineering and the Elmer and Sylvia Sramek Charitable Foundation. Scanning electron microscopy [NIH Shared Instrumentation Grant 1 S10 RR022498-01] was performed at the University of Iowa Central Microscopy Facility, a core resource supported by the Vice President for Research and Economic Development, the Holden Comprehensive Cancer Center and the Carver College of Medicine. Nuclear magnetic resonance was performed at the University of Iowa Central NMR Facility, which is supported by the NIH [S10-RR025500], the NSF [CHE-0840371] and University of Iowa funds. Sample sterilization for ISO 10993 testing was performed by the Holden Comprehensive Cancer Center Radiation and Free Radical Research (RFRR) Core for radiation services (supported by the Carver College of Medicine and NIH P30 CA086862). The authors would like to thank the staff at all three facilities for their assistance and support.

References

[1]. Aljohani W, Ullah MW, Zhang X, Yang G, Bioprinting and its applications in tissue engineering and regenerative medicine, Int J Biol Macromol 107(Pt A) (2018) 261–275. [PubMed: 28870749]

[2]. Worthington KS, Wiley LA, Bartlett AM, Stone EM, Mullins RF, Salem AK, Guymon CA, Tucker BA, Mechanical properties of murine and porcine ocular tissues in compression, Exp Eye Res 121 (2014) 194–9. [PubMed: 24613781]

[3]. Little CJ, Bawolin NK, Chen X, Mechanical properties of natural cartilage and tissue-engineered constructs, Tissue engineering. Part B, Reviews 17(4) (2011) 213–27. [PubMed: 21406046]

[4]. Kulkarni RK, Pani KC, Neuman C, Leonard F, Polylactic Acid for Surgical Implants, Arch Surg-Chicago 93(5) (1966) 839–1000. [PubMed: 5921307]

[5]. Burnight ER, Giacalone JC, Cooke JA, Thompson JR, Bohrer LR, Chirco KR, Drack AV, Fingert JH, Worthington KS, Wiley LA, Mullins RF, Stone EM, Tucker BA, CRISPR-Cas9 genome engineering: Treating inherited retinal degeneration, Prog Retin Eye Res 65 (2018) 28–49. [PubMed: 29578069]

[6]. Fernandez-Robredo P, Sancho A, Johnen S, Recalde S, Gama N, Thumann G, Groll J, Garcia-Layana A, Current Treatment Limitations in Age-Related Macular Degeneration and Future Approaches Based on Cell Therapy and Tissue Engineering, J Ophthalmol (2014).

[7]. Holz FG, Strauss EC, Schmitz-Valckenberg S, van Lookeren Campagne M, Geographic atrophy: clinical features and potential therapeutic approaches, Ophthalmology 121(5) (2014) 1079–91. [PubMed: 24433969]

[8]. Tomita M, Lavik E, Klassen H, Zahir T, Langer R, Young MJ, Biodegradable polymer composite grafts promote the survival and differentiation of retinal progenitor cells, Stem Cells 23(10) (2005) 1579–88. [PubMed: 16293582]

[9]. MacLaren RE, Pearson RA, MacNeil A, Douglas RH, Salt TE, Akimoto M, Swaroop A, Sowden JC, Ali RR, Retinal repair by transplantation of photoreceptor precursors, Nature 444(7116) (2006) 203–7. [PubMed: 17093405]

[10]. Klassen H, Sakaguchi DS, Young MJ, Stem cells and retinal repair, Prog Retin Eye Res 23(2) (2004) 149–81. [PubMed: 15094129]

[11]. Tao S, Young C, Redenti S, Zhang Y, Klassen H, Desai T, Young MJ, Survival, migration and differentiation of retinal progenitor cells transplanted on micro-machined poly(methyl methacrylate) scaffolds to the subretinal space, Lab on a chip 7(6) (2007) 695–701. [PubMed: 17538710]

[12]. Yao J, Ko CW, Baranov PY, Regatieri CV, Redenti S, Tucker BA, Mighty J, Tao SL, Young MJ, Enhanced Differentiation and Delivery of Mouse Retinal Progenitor Cells Using a Micropatterned Biodegradable Thin-Film Polycaprolactone Scaffold, Tissue Eng Pt A 21(7-8) (2015) 1247–1260.

[13]. Yao J, Tao SL, Young MJ, Synthetic Polymer Scaffolds for Stem Cell Transplantation in Retinal Tissue Engineering, Polymers-Basel 3(2) (2011) 899–914.

[14]. Kenawy ER, Abdel-Hay FI, El-Newehy MH, Wnek GE, Processing of polymer nanofibers through electrospinning as drug delivery systems, Mater Chem Phys 113(1) (2009) 296–302.

[15]. Shin M, Yoshimoto H, Vacanti JP, In vivo bone tissue engineering using mesenchymal stem cells on a novel electrospun nanofibrous scaffold, Tissue Eng 10(1-2) (2004) 33–41. [PubMed: 15009928]

[16]. Oh SH, Park IK, Kim JM, Lee JH, In vitro and in vivo characteristics of PCL scaffolds with pore size gradient fabricated by a centrifugation method, Biomaterials 28(9) (2007) 1664–71. [PubMed: 17196648]

[17]. Hutmacher DW, Schantz T, Zein I, Ng KW, Teoh SH, Tan KC, Mechanical properties and cell cultural response of polycaprolactone scaffolds designed and fabricated via fused deposition modeling, J Biomed Mater Res 55(2) (2001) 203–16. [PubMed: 11255172]

[18]. Siddiqui N, Asawa S, Birru B, Baadhe R, Rao S, PCL-Based Composite Scaffold Matrices for Tissue Engineering Applications, Mol Biotechnol (2018).

[19]. Bolgen N, Vargel I, Korkusuz P, Menceloglu YZ, Piskin E, In vivo performance of antibiotic embedded electrospun PCL membranes for prevention of abdominal adhesions, J Biomed Mater Res B Appl Biomater 81(2) (2007) 530–43. [PubMed: 17041925]

[20]. Bolgen N, Menceloglu YZ, Acatay K, Vargel I, Piskin E, In vitro and in vivo degradation of non-woven materials made of poly(epsilon-caprolactone) nanofibers prepared by electrospinning under different conditions, J Biomater Sci Polym Ed 16(12) (2005) 1537–55. [PubMed: 16366336]

[21]. Woodruff MA, Hutmacher DW, The return of a forgotten polymer-Polycaprolactone in the 21st century, Prog Polym Sci 35(10) (2010) 1217–1256.

[22]. Lee KH, Kim HY, Khil MS, Ra YM, Lee DR, Characterization of nano-structured poly(epsilon-caprolactone) nonwoven mats via electrospinning, Polymer 44(4) (2003) 1287–1294.

[23]. Sun H, Mei L, Song C, Cui X, Wang P, The in vivo degradation, absorption and excretion of PCL-based implant, Biomaterials 27(9) (2006) 1735–40. [PubMed: 16198413]

[24]. Jeong SI, Kim BS, Kang SW, Kwon JH, Lee YM, Kim SH, Kim YH, In vivo biocompatibilty and degradation behavior of elastic poly(L-lactide-co-epsilon-caprolactone) scaffolds, Biomaterials 25(28) (2004)5939–46. [PubMed: 15183608]

[25]. Christiansen AT, Tao SL, Smith M, Wnek GE, Prause JU, Young MJ, Klassen H, Kaplan HJ, la Cour M, Kiilgaard JF, Subretinal Implantation of Electrospun, Short Nanowire, and Smooth Poly(epsilon-caprolactone) Scaffolds to the Subretinal Space of Porcine Eyes, Stem Cells Int (2012).

[26]. Green BJ, Worthington KS, Thompson JR, Bunn SJ, Rethwisch M, Kaalberg EE, Jiao C, Wiley LA, Mullins RF, Stone EM, Sohn EH, Tucker BA, Guymon CA, Effect of Molecular Weight and Functionality on Acrylated Poly(caprolactone) for Stereolithography and Biomedical Applications, Biomacromolecules 19(9) (2018) 3682–3692. [PubMed: 30044915]

[27]. Sodha S, Wall K, Redenti S, Klassen H, Young MJ, Tao SL, Microfabrication of a three-dimensional polycaprolactone thin-film scaffold for retinal progenitor cell encapsulation, J Biomater Sci Polym Ed 22(4-6) (2011) 443–56. [PubMed: 20566039]

[28]. Cai S, Smith ME, Redenti SM, Wnek GE, Young MJ, Mouse retinal progenitor cell dynamics on electrospun poly (-caprolactone), J Biomater Sci Polym Ed 23(11) (2012) 1451–65. [PubMed: 21781383]

[29]. Sepahvandi A, Eskandari M, Moztarzadeh F, Fabrication and characterization of SrAl2O4: Eu(2+)Dy(3+)/CS-PCL electrospun nanocomposite scaffold for retinal tissue regeneration, Mater Sci Eng C Mater Biol Appl 66 (2016) 306–314. [PubMed: 27207067]

[30]. Zhang D, Ni N, Chen J, Yao Q, Shen B, Zhang Y, Zhu M, Wang Z, Ruan J, Wang J, Mo X, Shi W, Ji J, Fan X, Gu P, Electrospun SF/PLCL nanofibrous membrane: a potential scaffold for retinal progenitor cell proliferation and differentiation, Sci Rep 5 (2015) 14326. [PubMed: 26395224]

[31]. McHugh KJ, Tao SL, Saint-Geniez M, Porous poly(epsilon-caprolactone) scaffolds for retinal pigment epithelium transplantation, Invest Ophthalmol Vis Sci 55(3) (2014) 1754–62. [PubMed: 24550370]

[32]. Shahmoradi S, Yazdian F, Tabandeh F, Soheili ZS, Hatamian Zarami AS, Navaei-Nigjeh M, Controlled surface morphology and hydrophilicity of polycaprolactone toward human retinal pigment epithelium cells, Mater Sci Eng C Mater Biol Appl 73 (2017) 300–309. [PubMed: 28183612]

[33]. Taylor L, Arner K, Kolewe M, Pritchard C, Hendy G, Langer R, Ghosh F, Seeing through the interface: poly(epsilon-Caprolactone) surface modification of poly(glycerol-co-sebacic acid) membranes in adult porcine retinal explants, J Tissue Eng Regen Med 11(8) (2017) 2349–2358. [PubMed: 27098673]

[34]. Lance KD, Bernards DA, Ciaccio NA, Good SD, Mendes TS, Kudisch M, Chan E, Ishikiriyama M, Bhisitkul RB, Desai TA, In vivo and in vitro sustained release of ranibizumab from a nanoporous thin-film device, Drug Deliv Transl Res 6(6) (2016) 771–780. [PubMed: 27178165]

[35]. Wu W, He Z, Zhang Z, Yu X, Song Z, Li X, Intravitreal injection of rapamycin-loaded polymeric micelles for inhibition of ocular inflammation in rat model, Int J Pharm 513(1-2) (2016) 238–246. [PubMed: 27609662]

[36]. Lawley E, Baranov P, Young M, Hybrid vitronectin-mimicking polycaprolactone scaffolds for human retinal progenitor cell differentiation and transplantation, J Biomater Appl 29(6) (2015) 894–902. [PubMed: 25145988]

[37]. Curcio CA, Sloan KR, Packing geometry of human cone photoreceptors: variation with eccentricity and evidence for local anisotropy, Vis Neurosci 9(2) (1992) 169–80. [PubMed: 1504026]

[38]. Chui TYP, Song H, Burns SA, Individual variations in human cone photoreceptor packing density: Variations with refractive error, Invest Ophth Vis Sci 49(10) (2008) 4679–4687.

[39]. Chui TYP, Song HX, Clark CA, Papay JA, Burns SA, Elsner AE, Cone Photoreceptor Packing Density and the Outer Nuclear Layer Thickness in Healthy Subjects, Invest Ophth Vis Sci 53(7) (2012) 3545–3553.

[40]. Song HX, Chui TYP, Zhong ZY, Elsner AE, Burns SA, Variation of Cone Photoreceptor Packing Density with Retinal Eccentricity and Age, Invest Ophth Vis Sci 52(10) (2011) 7376–7384.

[41]. Bratton D, Yang D, Dai JY, Ober CK, Recent progress in high resolution lithography, Polym Advan Technol 17(2) (2006) 94–103.

[42]. Zhang YL, Chen QD, Xia H, Sun HB, Designable 3D nanofabrication by femtosecond laser direct writing, Nano Today 5(5) (2010) 435–448.

[43]. Sun HB, Kawata S, Two-photon photopolymerization and 3D lithographic microfabrication, Adv Polym Sci 170 (2004) 169–273.

[44]. Worthington KS, Wiley LA, Kaalberg EE, Collins MM, Mullins RF, Stone EM, Tucker BA, Two-photon polymerization for production of human iPSC-derived retinal cell grafts, Acta Biomater 55 (2017) 385–395. [PubMed: 28351682]

[45]. Wiley LA, Burnight ER, DeLuca AP, Anfinson KR, Cranston CM, Kaalberg EE, Penticoff JA, Affatigato LM, Mullins RF, Stone EM, Tucker BA, cGMP production of patient-specific iPSCs and photoreceptor precursor cells to treat retinal degenerative blindness, Sci Rep 6 (2016) 30742. [PubMed: 27471043]

[46]. Ross JW, Fernandez de Castro JP, Zhao J, Samuel M, Walters E, Rios C, Bray-Ward P, Jones BW, Marc RE, Wang W, Zhou L, Noel JM, McCall MA, DeMarco PJ, Prather RS, Kaplan HJ, Generation of an inbred miniature pig model of retinitis pigmentosa, Invest Ophthalmol Vis Sci 53(1) (2012) 501–7. [PubMed: 22247487]

[47]. Scott PA, de Castro JP, DeMarco PJ, Ross JW, Njoka J, Walters E, Prather RS, McCall MA, Kaplan HJ, Progression of Pro23His Retinopathy in a Miniature Swine Model of Retinitis Pigmentosa, Transl Vis Sci Technol 6(2) (2017) 4.

[48]. Tulig TJ, Tirrell M, Molecular theory of the Trommsdorff effect, Macromolecules 14(5) (1981) 1501–1511.

[49]. Sung HJ, Meredith C, Johnson C, Galis ZS, The effect of scaffold degradation rate on three-dimensional cell growth and angiogenesis, Biomaterials 25(26) (2004) 5735–42. [PubMed: 15147819]

[50]. Do AV, Worthington KS, Tucker BA, Salem AK, Controlled drug delivery from 3D printed two-photon polymerized poly(ethylene glycol) dimethacrylate devices, Int J Pharm 552(1–2) (2018) 217–224. [PubMed: 30268853]

[51]. Wiley LA, Burnight ER, Songstad AE, Drack AV, Mullins RF, Stone EM, Tucker BA, Patient-specific induced pluripotent stem cells (iPSCs) for the study and treatment of retinal degenerative diseases, Prog Retin Eye Res 44 (2015) 15–35. [PubMed: 25448922]

[52]. Meyer JS, Howden SE, Wallace KA, Verhoeven AD, Wright LS, Capowski EE, Pinilla I, Martin JM, Tian S, Stewart R, Pattnaik B, Thomson JA, Gamm DM, Optic vesicle-like structures derived from human pluripotent stem cells facilitate a customized approach to retinal disease treatment, Stem Cells 29(8) (2011) 1206–18. [PubMed: 21678528]

[53]. Meyer JS, Shearer RL, Capowski EE, Wright LS, Wallace KA, McMillan EL, Zhang SC, Gamm DM, Modeling early retinal development with human embryonic and induced pluripotent stem cells, Proc Natl Acad Sci U S A 106(39) (2009) 16698–703. [PubMed: 19706890]

[54]. Ohlemacher SK, Iglesias CL, Sridhar A, Gamm DM, Meyer JS, Generation of highly enriched populations of optic vesicle-like retinal cells from human pluripotent stem cells, Curr Protoc Stem Cell Biol 32 (2015) 1H 8 1-20.

[55]. Zhong X, Gutierrez C, Xue T, Hampton C, Vergara MN, Cao LH, Peters A, Park TS, Zambidis ET, Meyer JS, Gamm DM, Yau KW, Canto-Soler MV, Generation of three-dimensional retinal tissue with functional photoreceptors from human iPSCs, Nat Commun 5 (2014) 4047. [PubMed: 24915161]

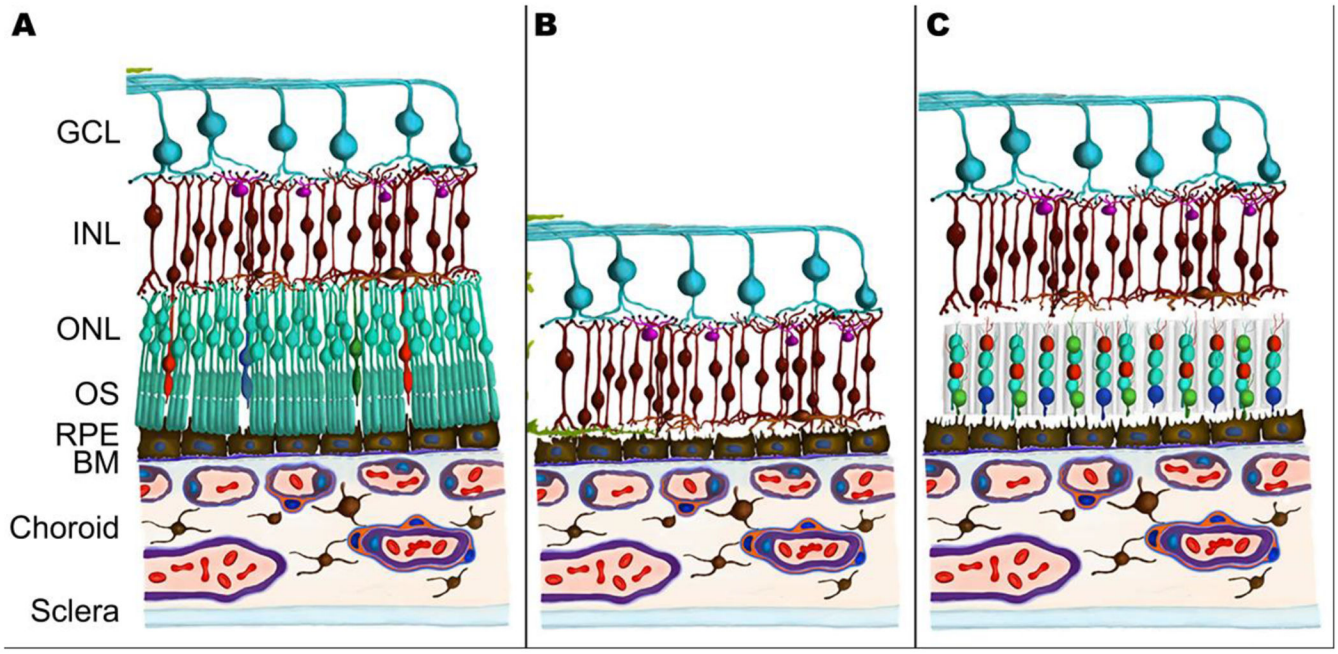

Figure 1.

Schematic of scaffold-assisted retinal regeneration. Compared to a healthy retina (A), a retina affected by late-stage inherited or age-related degeneration encounters a loss of photoreceptor cells (B). Our objective in this study is to create a biodegradable, precisely structured scaffold that could be used to deliver replacement photoreceptor cells (C). GCL: Ganglion Cell Layer; INL: Inner Nuclear Layer; ONL: Outer Nuclear Layer; OS: Outer Segments; RPE: Retinal Pigment Epithelium; BM: Bruch's Membrane.

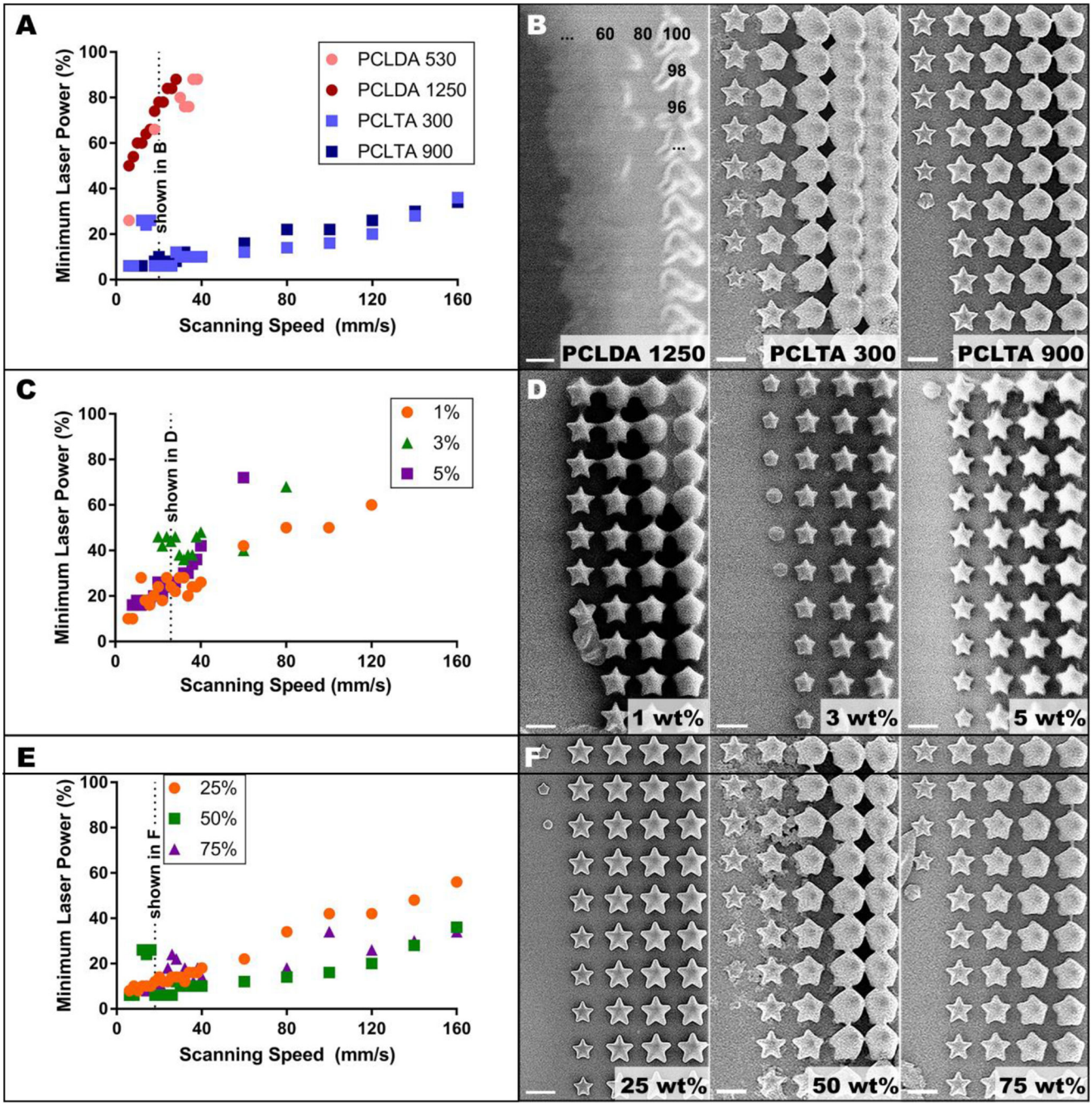

Figure 2.

Two-photon polymerization threshold. A) Threshold profiles for four acrylated PCL prepolymers at fixed composition (50 wt% monomer, 3 wt% photoinitiator) with B) corresponding images of stars fabricated at 20 mm/s. The numbers in sub-panel i indicate the laser power used at each star position. C) Threshold profiles for three photoinitiator concentrations in 50 wt% 900 g/mol PCLTA with D) corresponding images of stars of the same composition at 26 mm/s. E) Threshold profiles for three concentrations of 300 g/mol PCLTA with 3 wt% photoinitiator and F) corresponding images of stars of the same

composition at 18 mm/s. Scale bars in B, D and F represent 10 μm. In all threshold profiles, each datapoint represents a single laser power value, below which polymerized structures were not observed, and above which polymerized structures were consistently observed.

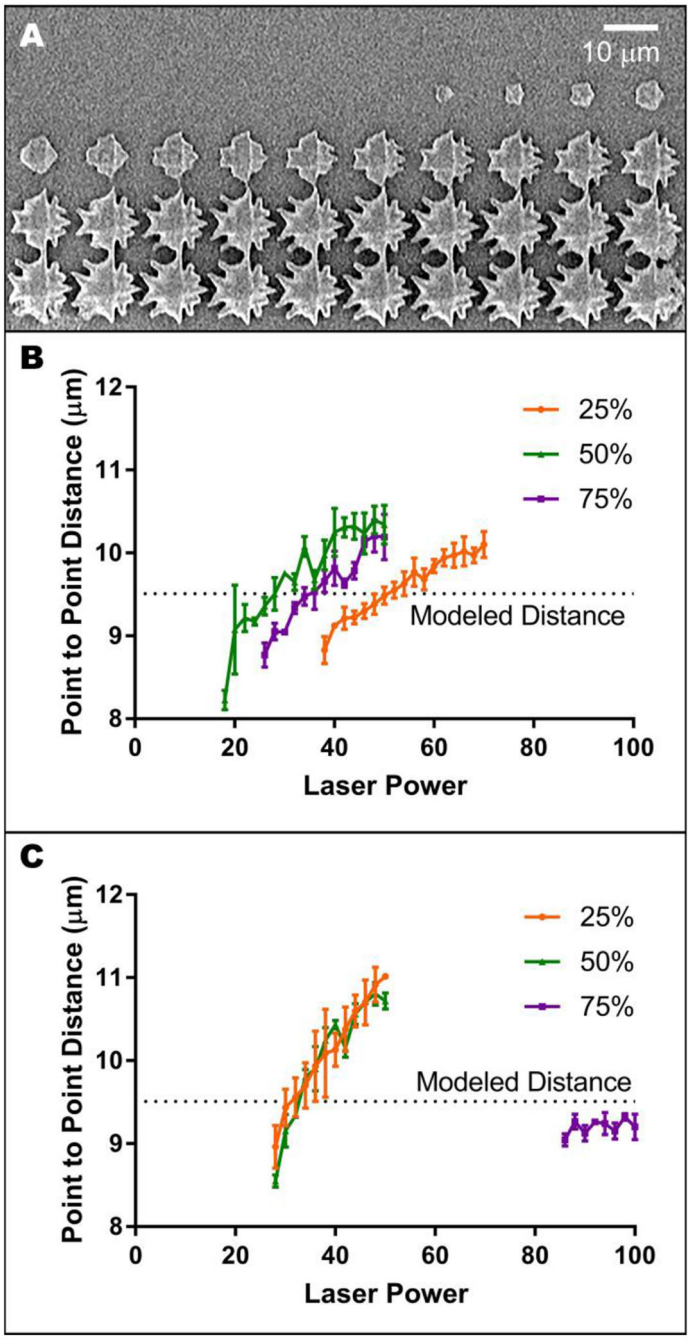

Figure 3.

Determining optimal laser power and scanning speed. A) Representative image of undesirable, delaminated two-photon polymerized structures. B-C) Width of stars created using the fastest scanning speed that did not result in edge artifacts for 300 g/mol (B) and 900 g/mol (C) PCLTA at three prepolymer concentrations, each with 3 wt% photoinitiator. Each point represents the mean (n = 3), while error bars represent the standard deviation and the dotted line represents modeled star pointtopoint distance.

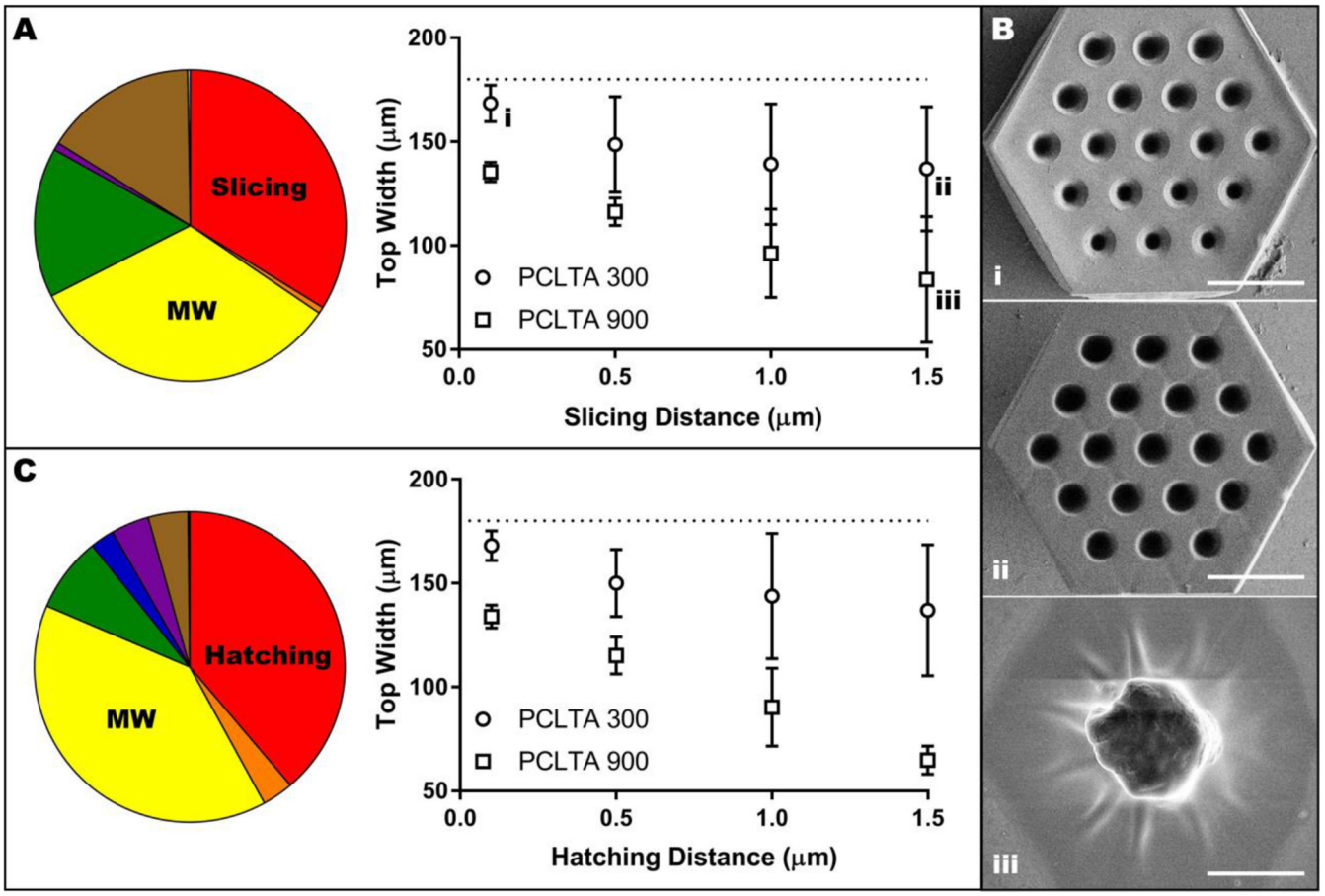

Figure 4.

Influence of slicing distance, hatching distance and molecular weight on scaffold width. A) Pie chart representing the contribution of experimental variables on scaffold width with constant hatching of 0.5 μm and a consolidated graphical analysis showing only the effect of slicing distance and molecular weight (data points were averaged across all polymer concentrations). Lower case Roman numerals are a cross-reference to Panel B. B) Representative images of the effect of slicing distance and molecular weight on the width of PCL scaffolds: 300 g/mol with 0.1 μm slicing distance (i), 300 g/mol with 1.5 lm slicing distance (ii), and 900 g/mol with 1.5 μ m slicing distance with all other variables held at 75 wt% prepolymer and 0.5 μ m hatching distance. Scale bars represent 50 μm. C) Pie chart representing the contribution of experimental variables on scaffold width with constant slicing of 0.5 μm and a consolidated graphical analysis showing only the effect of hatching distance and molecular weight (data points were averaged across all polymer concentrations). In A and C, the dotted line indicates the designed width of 180 μm and the colors represent the following variables: red, slicing or hatching distance; orange, interaction between slicing or hatching distance and molecular weight; yellow, molecular weight; green, interaction between molecular weight and prepolymer concentration; blue, prepolymer concentration; purple, interaction between prepolymer concentration and slicing or hatching distance; brown, interaction between slicing or hatching distance, molecular weight and prepolymer concentration; grey, other.

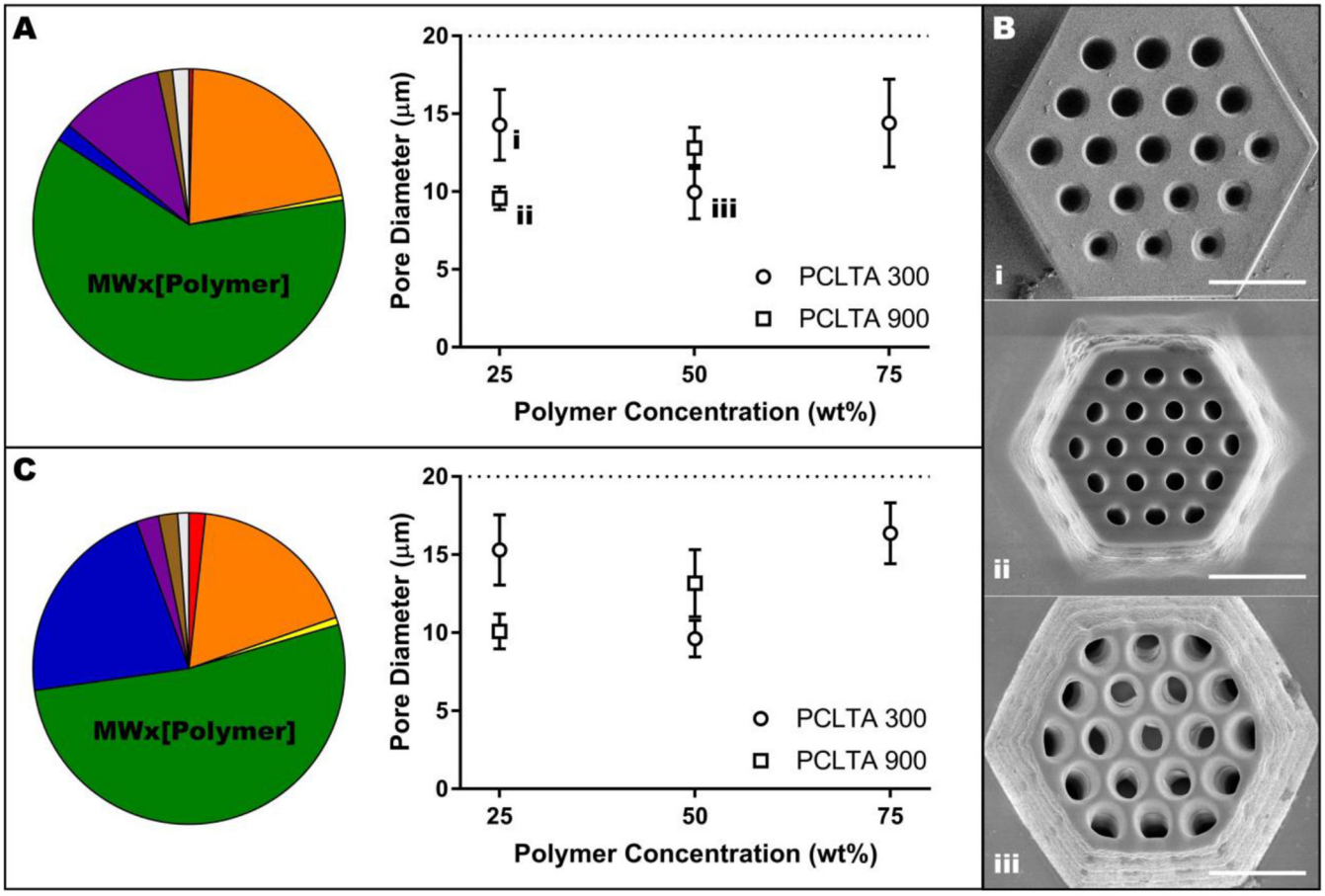

Figure 5.

Influence of molecular weight and prepolymer concentration on the vertical pore diameter of PCLTA scaffolds. A) Pie chart representing the contribution of experimental variables on pore diameter with constant hatching distance of 0.5 μm and a consolidated graphical analysis showing only the effect of molecular weight and prepolymer concentration (data points were averaged across all hatching distances). Lower case Roman numerals are a cross-reference to Panel B. B) Representative images of the effect of molecular weight and prepolymer concentration on pore diameter: 25 wt% 300 g/mol (i), 25 wt% 900 g/mol (ii) and 50 wt% 300 g/mol (iii) with all other variables held at 1.5 μm slicing distance and 0.5 μm hatching distance. Scale bars represent 50 μm. C) Pie chart representing the contribution of experimental variables on pore diameter with constant slicing distance of 0.5 μm and a consolidated graphical analysis showing only the effect of molecular weight and prepolymer concentration (data points were averaged across all slicing distances). In A and C, the dotted line indicates the designed pore diameter of 20 μm and the colors represent the following variables: red, slicing or hatching distance; orange, interaction between slicing or hatching distance and molecular weight; yellow, molecular weight; green, interaction between molecular weight and prepolymer concentration; blue, prepolymer concentration; purple, interaction between prepolymer concentration and slicing or hatching distance; brown, interaction between slicing or hatching distance, molecular weight and prepolymer

concentration; grey, other. (For interpretation of the references to color in this figure legend, the reader is referred to the web version of this article.)

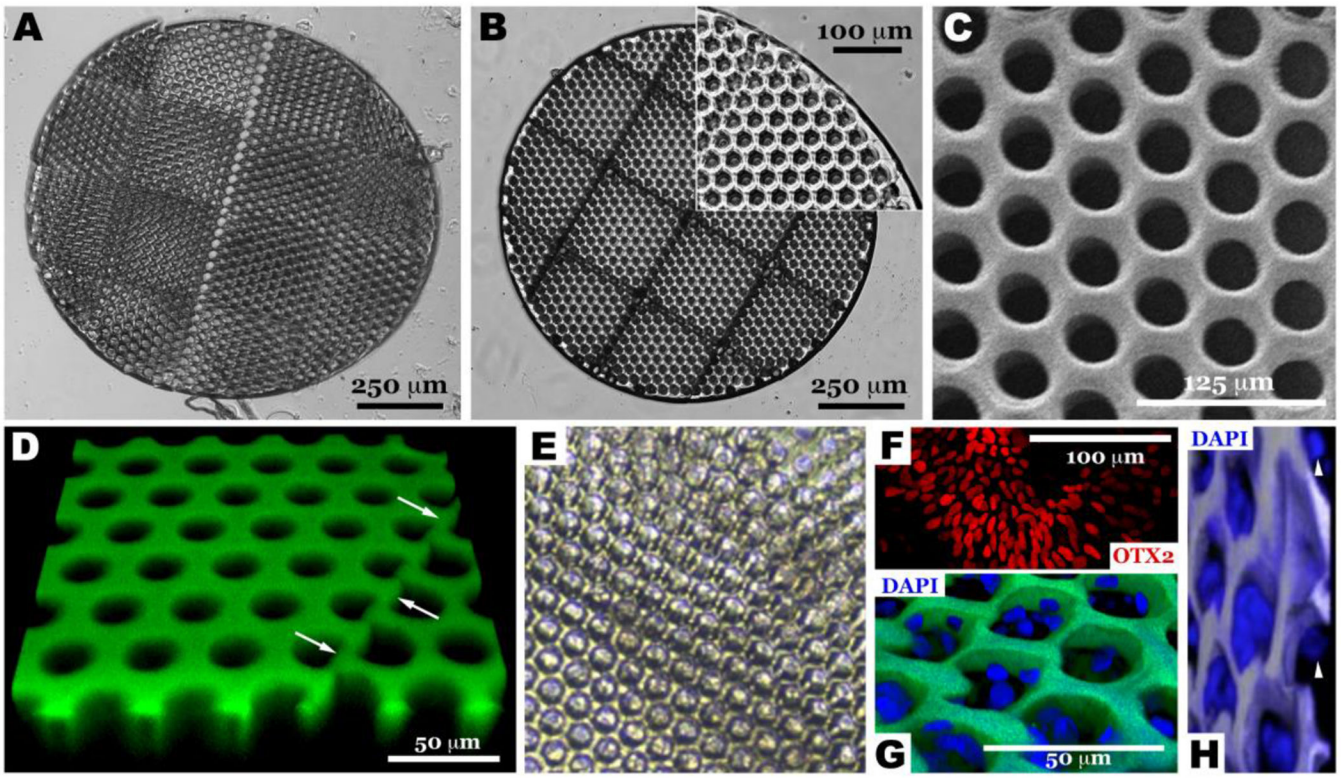

Figure 6.

Scale-up and validation of optimized two-photon polymerization to transplantation relevant size. Light micrographs of scaffolds created using 75 wt% 300 g/mol PCLTA with slicing and hatching distances of either 1.5 μm (A) or 1.0 μm (B). Further imaging of the 1.0 μm slicing and hatching sample previously described, using SEM (C) and confocal microscopy (D, polymer autofluorescent when excited with 488 nm laser). Light (E) and confocal micrographs (G & H) of two-photon polymerized PCL scaffold seeded with human iPSC derived OTX2-positive retinal progenitor cells (F). The presence of iPSC derived retinal progenitor cells within two-photon polymerized scaffolds at 9-days post-seeding indicate a lack of acute toxicity induced by residual pre-polymer and/or processing reagents (E, G & H). Arrows in panel D indicate the stitch line created during scaffold scale-up. Arrowheads in panel H point to cells at the bottom of the vertical pores to the immediate left, indicating that the pore is filled with cells one on top of the other from the top of the scaffold to the bottom.

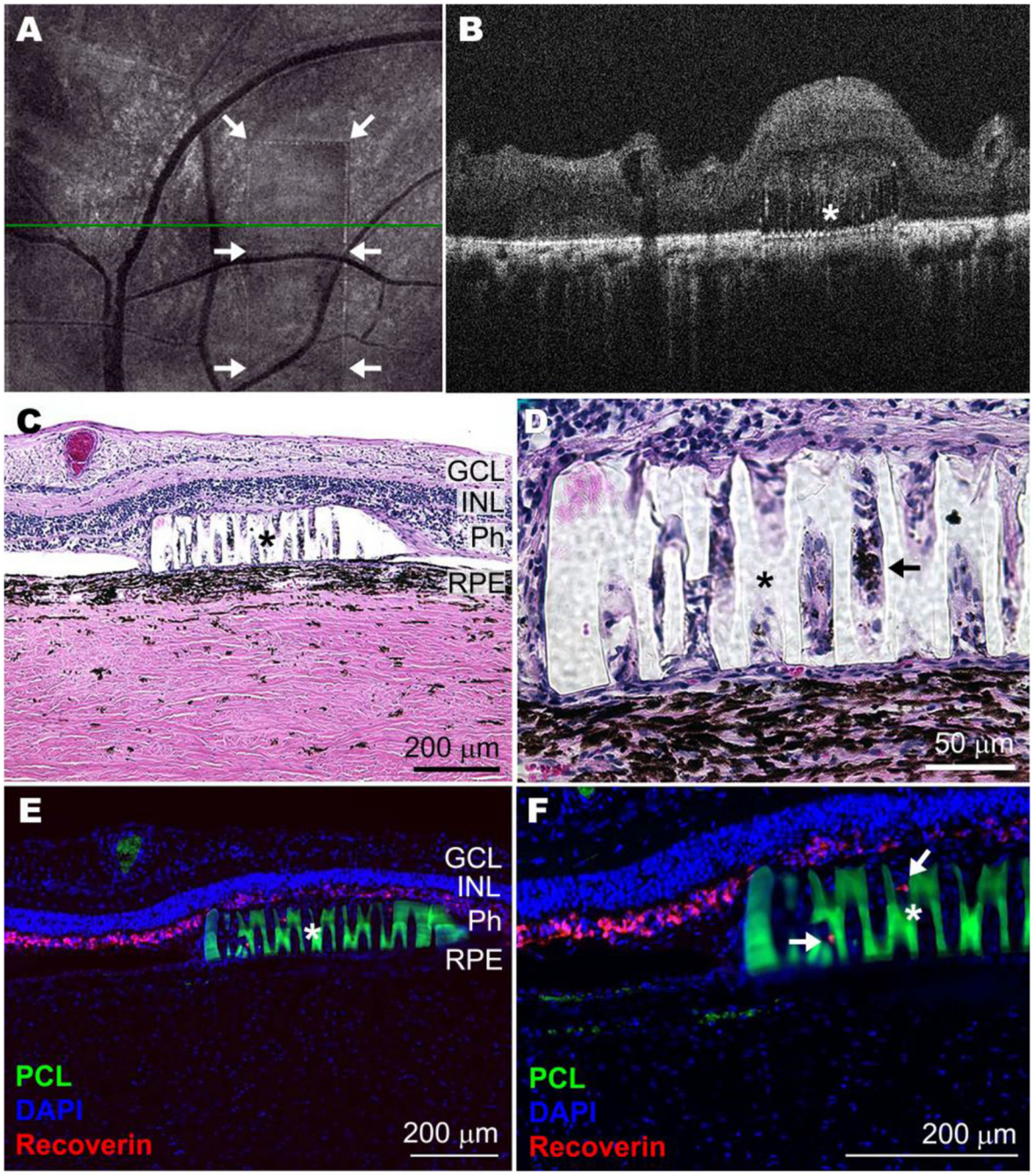

Figure 7.

Scaled-up prototype of crosslinked PCLTA 900 in the degenerating pig sub-retinal space 30 days after transplantation. Representative en face (A) and horizontal B-scan (B) optical coherence tomographs (green line in A indicates cross-sectional plane shown in B) of the post-mortem Pro23His pig eye show placement of the transplanted polymer (border indicated with arrows in A and marked with * in B). Representative histological (C and D) and immunohistochemical (E and F) images of retinal sections (RPE: retinal pigment epithelium; Ph: photoreceptor cells; INL: inner-nuclear layer; GCL: ganglion cell layer)

show the embedded PCL scaffolds (marked with * and in E and F also autofluorescent in green) and surrounding tissue with some presumptive RPE cells (pigmented, shown with arrow in D) and photoreceptor cells (Recoverin positive, shown with arrows in F) infiltrating the scaffold. (For interpretation of the references to color in this figure legend, the reader is referred to the web version of this article.)

Table 1.

Optimal scanning speeds and laser powers for PCLTA formulations with 3 wt% photoinitiator.

Molecular Weight (g/mol)	[Polymer] (wt%)	Scanning Speed (mm/s)	Laser Power (%)
300	25	36	50
	50	40	28
	75	40	36
900	25	60	32
	50	60	32
	75	18	100

Table 2.

ISO 10993 cytotoxicity, genotoxicity, pyrogenicity, sensitization, subtoxicity, and systemic toxicity testing.

Target	Assay	Outcome
Cytotoxicity	MEM Elution Using Mouse Fibroblast Cells (GLP)	Negative
Genotoxicity	In Vitro Mouse Lymphoma with Extended Treatment (GLP)	Negative
	Bacterial Mutagenicity - Ames Assay (GLP)	Negative
Pyrogenicity	Materials-Mediated Rabbit Pyrogen (GLP)	Negative
Sensitization	Guinea Pig Maximization Sensitization (GLP)	Negative
Sub-Toxicity	Subchronic IV Toxicity with Histopathology, Clinical Chemistry & Hematology - 14 Day - 14 Dose - Mice (GLP)	Negative
	Subacute IP Toxicity with Histopathology, Clinical Chemistry & Hematology - 14 Day - 14 Dose - Mice (GLP)	Negative
Systemic	Acute Systemic Toxicity (GLP)	Negative

Table 3.
Toxicological risk assessment, component extraction.

GC-MS: Gas Chromatography-Mass Spectrometry, LC-MS: Liquid Chromatography-Mass Spectrometry, ICP-MS: Inductively Coupled Plasma Mass Spectrometry, HS-GC-MS: Headspace Gas Chromatography-Mass Spectrometry, MOS: Margin of safety.

Assay	100% exposure in 24 hrs	100% exposure over 30 days
GC-MS in hexane extracts	Negative	N/A
GC-MS in IPA/water extracts	Negative	N/A
GC-MS in water extracts	Negative	N/A
LC-MS in hexane extracts	Negative	N/A
LC-MS in IPA/water extracts	27 negative, 1 positive *	Negative
LC-MS in water extracts	19 negative, 1 positive *	Negative
ICP-MS	Negative	N/A
HS-GC-MS	Negative	N/A

* Trimethylolpropane monoacrylate, MOS < 1.